

STRATEGIES FOR COMPUTING THE SCALAR SELF-FORCE ON A
SCHWARZSCHILD BACKGROUND: A COMPARISON STUDY WITH AN FORTRAN
CODE IN C++, EXTRAPOLATING TO INFINITE DISCONTINUOUS GALERKIN
ORDER, AND EXTRAPOLATING TO INFINITE SPHERICAL HARMONIC MODES

A Thesis/Dissertation

Submitted to the Graduate Faculty of the
Louisiana State University and
Agricultural and Mechanical College
in partial fulfillment of the
requirements for the degree of
Master of Science

in

Physics

by

Steven (Susan) Dorsher

B.S., Massachusetts Institute of Technology, 2004

M.S., The Ohio State University, 2006

M.S., University of Minnesota, 2013

December, 2017

Acknowledgments

I would like to thank Peter Diener and Frank Löffler for their guidance. Peter Diener especially has been very important to me, both as an advisor and personally. I would also like to thank Gabriela Gonzalez for the excellent opportunity to work on LIGO during the time of three detections, which provided me the funding I needed to continue the work detailed in this document. I would like to thank Juana Moreno for the opportunity to work as outreach coordinator to the LA-SIGMA Research Experience for Undergraduates program my first summer at LSU, which also helped provide funding for this research. My parents, Paul and Joanne Dorsher, also deserve a mention, both for extraordinary moral support and for the financial support they provided that helped make this possible. I would also like to thank my sister Patricia Dorsher, my grandmother Evie Dorsher and her sister Gwen Helbling, and my Aunt Peggy Bennett, and my Aunt Elaine Shirley for being my anchor. I would like to thank my friends Christy Paulson, Hope Ring, Steve Brandt, Brad Schaefer, Luke, and Josh McKeown for their company and kindness during this process. My family, friends, and loved ones are the purpose behind this work.

Table of Contents

ACKNOWLEDGMENTS	ii
LIST OF TABLES	v
LIST OF FIGURES	vi
ABSTRACT	x
CHAPTER	
1 INTRODUCTION	1
1.1 Gravitational Waves	1
1.2 Extreme Mass Ratio Inspirals	2
1.3 EMRIs	2
1.4 The discontinuous galerkin method	2
1.5 LISA	2
1.6 Notation	2
2 A SIMPLE NUMERICAL SOLUTION FOR A PDE USING THE DISCONTINUOUS GALERKIN METHOD	4
2.1 Reduction to coupled first order differential equations	4
2.2 Method of Lines	5
2.2.1 Spatial grids	5
2.2.2 Time evolution	8
2.3 Wave equation on flat spacetime	8
3 A SCALAR FIELD ON A SCHWARZSCHILD BACKGROUND WITHOUT A SOURCE	12
3.1 Scalar field on Schwarzschild spacetime	12
3.1.1 Scalar field wave equations	12
3.2 Theoretical expectations	15
3.2.1 Quasinormal modes	17
3.2.2 Power law tails	18
4 CIRCULAR ORBITS ON A SCHWARZSCHILD SPACETIME	21
4.1 Self Force	21
4.1.1 World tube	23
4.2 Comparison between C++ and Fortran codes	23
5 ELLIPTICAL ORBITS ON A SCHWARZSCHILD SPACETIME	26
5.1 Orbital parameters (osculating orbits paper)	26
5.2 Time dependent coordinate transformation	27
5.3 Orbbits	29
5.4 Self Force	29

6	EXTRAPOLATING THE SELF FORCE TO INFINITE DISCONTINUOUS GALERKIN ORDER	32
6.0.1	Checking for discontinuities in F_{inf} for each each l-mode	32
6.0.2	Determining F_{inf} using maximum likelihood fits to subsegments of lines in semilog space	33
7	EXTRAPOLATING THE MODE-SUMMED SELF-FORCE TO INCLUDE CONTRIBUTIONS FROM AN INFINITE NUMBER OF SPHERICAL HARMONIC MODES.....	42
7.0.1	Fractional errors.....	44
7.0.2	Structure of the error compared to the evolu- tion in time	44
8	IMPROVING MODE FITS VIA A POWER LAW SCALED WEIGHT FACTOR IN χ^2 SUM	52
8.0.1	Relative error as a function of mode	52
8.1	ToDO	52
9	FUTURE WORK: GENERIC ORBITS VIA THE OSCU- LATING ORBITS FRAMEWORK.....	56
9.1	plans for the future	56
9.2	Generic orbits	56
9.2.1	Geodesic evolution	56
9.2.2	Osculating orbits	56
9.2.3	methods	56
	REFERENCES.....	57
	VITA	61

List of Tables

6.1	Manual starting indices and F_{inf} values for $t=632$, $l=2$	32
-----	---	----

List of Figures

2.1	Waves evolving over time for gaussian initial conditions	9
2.2	Waves evolving over time for sinusoidal initial conditions	10
2.3	L_2 error scaling with DG order for sinusoidal initial conditions	10
2.4	L_2 error scaling with element size for sinusoidal initial conditions	11
3.1	Scalar field spatial slice initial condition and first full timestep for $l=0$	16
3.2	Time derivative of the scalar field spatial slice initial condition and first full timestep for $l=0$	16
3.3	Radial derivative of the scalar field spatial slice initial condition and first full timestep for $l=0$	17
3.4	Quasinormal mode for $l=1, m=1$	18
3.5	Quasinormal mode for $l=2, m=2$	19
3.6	Power law tail, $l=1, m=1$	19
3.7	Power law tail does not match expectations due to truncation error in DG method, $l=2, m=2$	20
4.1	Spatial slice of the world tube window function.	22
4.2	Comparison between Fortran and C++ codes for a particle on a circular orbit, $l=0, m=0$	24
4.3	Comparison between Fortran and C++ codes for a particle on a circular orbit, $l=1, m=1$	24
4.4	Comparison between Fortran and C++ codes for a particle on a circular orbit, $l=2, m=0$	25
4.5	Comparison between Fortran and C++ codes for a particle on a circular orbit, $l=2, m=2$	25
5.1	Schwarzschild r as a function of time over several orbits.	27
5.2	With χ as the angle in polar coordinates, the orbit forms an ex- act ellipse. This is the definition of χ , provided r is in Schwarzschild coordinates. Shown for $p = 9.9$ and $e = 0.1$, DG order 44.	28

5.3	The orbit as it physically would exist, using Schwarzschild ϕ as the polar coordinate angle. The orbit precesses but does not inspiral since there is no generic evolution. Shown for $p = 9.9$ and $e = 0.1$, DG order 44.....	28
5.4	Precession of the elliptical orbit is demonstrated due to the inequality in the period of the angular variables χ , which represents the period of the radial oscillations, and ϕ , which represents the period of the angular oscillations. $p = 9.9$, $e = 0.1$, DG order 44.....	29
5.5	Raw output of Diener, Warburton, and Wardell code for DG order 44. Radial self force.....	30
5.6	Raw output of Diener, Warburton, and Wardell code for DG order 44. Time component of the self force.	30
5.7	Raw output of Diener, Warburton, and Wardell code for DG order 44. Phi component of the self force.....	31
6.1	$g(\alpha)$	33
6.2	DG convergence with order, extrapolated from highlighted points to infinite order along exponential form, which appears as a straight line in the semilog plot.	34
6.3	Starting order was chosen by iterating from the lowest order to the first order for which the “mode failed”, and choosing the maximum starting order that succeeded. When F_{inf} is evolved over one full orbital cycle, some l-modes shows discontinuities at some times. l=3	35
6.4	Fluctuation in one of the points chosen in the extrapolation, due to roundoff or truncation error, causes the extrapolation to predict a value of F_{inf} that is subtly wrong, leading to curvature in the semilog plot after F_{inf} subtraction. t=632, l=2, i=1	36
6.5	Roundoff error is visible at high DG orders. t=632, l=2, i=2	37
6.6	The incorrect value of F_{inf} has been chosen due to roundoff error, perhaps due to finite precision in the root finding algorithm, leading to a negative values, that show as a “V” in the semilog plot. t=632, l=3, i=3	38
6.7	Manual correction for the discontinuities in the l=2 mode, using the manually determined F_{inf} data from Table 6.1.	39

6.8	An example of no discontinuities in F_{inf} for any of the l-modes. Mode $l = 0$	40
6.9	$l=0$ mode with line-segment fit-chosen starting order produces convergence plot with long exponentially converging region	41
7.1	Three term fit of l-mode vs F_{inf} . Note how the fit is bad at high l. There are an infinite number of additional terms that can be added to the fit to account for this deviation. However, it is also fundamentally difficult to fit an exponentially converging function. See Chapter 8.1.	43
7.2	This is the actual summed, doubly extrapolated, radial self force, measured in three different ways as described in the three figures above.	44
7.3	$t=635$, 2, 3, and 4 term fits over a broad range of lmin and lmax values. Note the roundoff noise at high lmax. Aphelion, where this effect is worst.	45
7.4	$t=635$, 2, 3, and 4 term fits over a small range of lmin and lmax. This is the actual range used to estimate the total self force. Aphelion, where the roundoff noise is worst. Note that there is not a large difference between two and three terms, and that four terms is less smooth a surface, suggesting that it is more subject to round off noise. Three terms is preferred.	46
7.5	This is the relative difference between the total radial self force measured in two different ways. In both cases, the self force was extrapolated to infinite order at every l-mode at every possible DG starting order. The infinite DG order self forces over the var- ious starting orders were sorted, eliminating NaNs. The median was chosen for each l-mode. Then the self force as a function of l-mode was fit to its three term form, and the sum was summed from zero to lmax, then extrapolated from $lmax + 1$ to infin- ity using an analytic form determined using Mathematica. All possible choices with lmin between 14 and 17 and lmax between 22 and 25 were averaged to obtain the total radial self force as a function of time. Similarly, all possible choices with lmin be- tween 14 and 19 and lmax between 24 and 30 were averaged to obtain the total radial self force as a function of time. This plot shows the relative difference. I believe the smaller range is in the denominator.	47

7.6	This figure was produced in the same manner as the previous figure, averaging over the smaller range, only it is a comparison between including either two or three terms in the l-mode fit. I believe the three term fit is in the denominator of the relative difference.....	48
7.7	This figure was produced in a similar manner to the first figure, only instead of using the median, it is a comparison between using the median, the maximum, and the minimum. The purple line is the relative difference between the maximum and the median, which is subject to roundoff error due to the potential for the maximum to contain roundoff error. The green line is the relative difference between the median and the minimum, which is subject to effects due to failure to converge. I suspect the median is the best compromise between these two effects, rejecting outliers in both directions, though it is a simplistic approach to doing so, and does not guarantee success. It is possible to have a starting order that has not converged and is also in the roundoff regime, for example. A better guarantee of success, though not a certain one, would be to do a fit over part of the error convergence plot to determine exponentiality, by fitting a line in semilog scale. However, this seems unnecessarily complex at this time.....	49
7.8	3 term, median method.....	50
7.9	3 term, fit method.....	50
7.10	The structure of the absolute error in comparison to the evolution in time for the fit method.....	51
8.1	$t=570$, $l=1$, three term fit with two different power law scales for weights in comparison to unscaled weights ($\sigma = 1$).	53
8.2	The difference between the triangles and the circles shows that the difference in the total radial self force between the presence of a $\sigma \sim l^{-2}$ weight and no weight is unimportant compared to the difference in the total radial self force between various start and end points of the l-mode fit.....	54
8.3	Absolute error between fit and median techniques increases with l-mode, explaining why the difference between weight and no weight fit techniques is unimportant.....	55

Abstract

Insert the text of your abstract here. Make sure there is one blank line between the end of the Abstract text and the “end” command below to maintain double-spaced lines.

Chapter 1

Introduction

1.1 Gravitational Waves

On February 11, 2016, the LIGO Scientific Collaboration announced the first detection of gravitational waves from a black hole binary inspirals, occurring on September 14, 2015, with pre-merger masses of $36 M_{\odot}$ and $29 M_{\odot}$ and a post merger mass of $62 M_{\odot}$ at a redshift of $z = 0.09$ [34]. Two subsequent detections followed, on December 26, 2015 [35] and on January 4, 2017 [36], with masses that are about the same to within an order of magnitude.

There is a question of what is meant, observationally, by a black hole. Does it need to have a horizon? Does it need to have a Kerr metric (the simplest possible space-time for a spinning black hole in general relativity)? Does it simply need to be a sufficiently compact object that it can't be ordinary nuclear matter? Historically, black holes have been defined by their compactness [48]; however, some studies are beginning to consider tests of horizons [] or of the Kerr metric itself [48]. X-ray binaries, gravitational wave constraints from binary-pulsar systems, active galactic nuclei models containing super-massive black holes on the order of $10^6 M_{\odot}$, and the three LIGO detections, as well as black hole formation models, suggest that black holes of all scales should be spinning [48]. However, for the purposes of this manuscript, I will consider non-spinning, spherically symmetric black holes in general relativity, described by the Schwarzschild metric.

Currently, there are four distinct windows on the gravitational wave universe planned or in progress. The Laser Interferometer Gravitational Wave Observatory, LIGO, probably deserves first listing, due to their recent success. LIGO observes gravitational waves using a ground based Michelson-Morley interferometer with two 4 kilometer long Fabry-Perot cavity arms. It detects strains as small as $10^{-23} Hz^{-1/2}$ [49].

1.2 Extreme Mass Ratio Inspirals

1.3 EMRIs

1.4 The discontinuous galerkin method

1.5 LISA

1.6 Notation

In this manuscript, I use Einstein summation notation for tensors, where a repeated Greek index implies a summation over that repeated index. For example, an n dimensional tensor field of rank (1,2) transforms, in general, according to the rule

$$T_{\beta\gamma}^{\alpha}(\bar{x}^1, \dots, \bar{x}^n) = \Lambda_{\delta}^{\alpha} \Lambda_{\beta}^{\epsilon} \Lambda_{\gamma}^{\zeta} T_{\epsilon\zeta}^{\delta}(x^1, \dots, x^n) \quad (1.1)$$

where Λ is the jacobian of the coordinate transformation from x to \bar{x} .

Indices are raised by use of the inverse metric and lowered by use of the metric. The metric transforms contravariant one-forms, which constitute the basis, to covariant vectors, which constitute the coordinates, e.g. $u^{\beta} = g^{\alpha\beta} u_{\alpha}$, where $g^{\alpha\beta}$ is the metric. However, the metric and its inverse can also be used to raise and lower indices of tensors of higher and mixed rank. The metric describes the relative distance between two coordinates on a manifold, in all n dimensions, in an $n \times n$ matrix. Two sign conventions are allowed, depending on whether the time component is positive or negative, though the metric always has a negative determinant in four dimensions. In our sign convention, the Minkowski metric for flat spacetime is given by

$$\eta^{\mu\nu} = \begin{bmatrix} -1 & 0 & 0 & 0 \\ 0 & 1 & 0 & 0 \\ 0 & 0 & 1 & 0 \\ 0 & 0 & 0 & 1 \end{bmatrix}$$

Here the four dimensions are Cartesian, t , x , y , and z . The Schwarzschild metric for a spherically symmetric blackhole without charge or spin is given by

$$d\tau^2 = g^{\mu\nu} \begin{bmatrix} -(1 - \frac{2M}{r}) & 0 & 0 & 0 \\ 0 & (1 - \frac{2M}{r})^{-1} & 0 & 0 \\ 0 & 0 & r^2 & 0 \\ 0 & 0 & 0 & r^2 \sin^2 \theta \end{bmatrix}$$

where $d\tau$ is the proper time, and coordinates are t (the local time), r (a radial coordinate that goes to zero at the singularity, $2M$ at the horizon, and infinity at spatial infinity), θ (the polar angle), and ϕ (the azimuthal angle). To obtain the inverse (lowered) metric, simply invert the matrix representation.

Chapter 2

A simple numerical solution for a PDE using the Discontinuous Galerkin method

2.1 Reduction to coupled first order differential equations

The fundamental problem we wish to solve is to evolve the wave equation on Schwarzschild spacetime with a source. However, to begin to address this problem, I implemented a one dimensional wave equation solver in C++ using the Discontinuous Galerkin method in flat spacetime. The wave equation in flat spacetime is given, in several different forms, by

$$\square\psi = 0 \tag{2.1}$$

$$\frac{\partial^2\psi}{\partial t^2} = \nabla\psi \tag{2.2}$$

$$\frac{\partial^2\psi}{\partial t^2} = \frac{\partial^2\psi}{\partial r^2} \tag{2.3}$$

where the final form is specialized to one dimension. To numerically integrate this, it is necessary to reduce this second order differential equation to three coupled differential first order differential equations. There is a classical solution to this problem, which we follow. We introduce variables $\rho = \frac{\partial\psi}{\partial t}$ and $\phi = \frac{\partial\psi}{\partial r}$. With these definitions, and remembering that we want time evolution equations rather than spatial evolution equations, the three coupled equations become

$$\frac{\partial\psi}{\partial t} = \rho \tag{2.4}$$

$$\frac{\partial\rho}{\partial t} = \frac{\partial\phi}{\partial r} \tag{2.5}$$

$$\frac{\partial\phi}{\partial t} = \frac{\partial\rho}{\partial r} \tag{2.6}$$

This system of equations can be rewritten

$$\frac{\partial u}{\partial t} = A \frac{\partial u}{\partial r} + B \frac{\partial u}{\partial t} = RHS(u, t)$$

where u is the state vector consisting of $u = (\psi, \rho, \phi)$, and A and B are matrices. RHS stands for Right Hand Side. The C++ code has been implemented for wave equations of this generalized form, which encompasses wave equations on a Schwarzschild spacetime.

2.2 Method of Lines

The method of lines is a method for solving partial differential equations in which spatial dimensions are discretized and time (conventionally) is evolved with numerical integration. We use this technique to solve the wave equation.

2.2.1 Spatial grids

Our code solves a wave equation, which must first calculate a spatial derivative then integrate in time to solve a differential equation. For the spatial derivative part of the scheme, we make use of the Discontinuous Galerkin method to compute spatial derivatives, as a replacement for a finite difference scheme. It has three primary benefits. One is that it naturally handles discontinuities in the evolved field, which is important to the effective source approach that we use when calculating orbits with a source in curved spacetime. The second is that its accuracy scales exponentially with increasing polynomial order. The third is that its accuracy scales as a power law with decreasing element size, giving a second strong way to reduce the truncation error.

- **Finite difference schemes**

The classic solution to the spatial derivative problem is the finite difference scheme. In a one dimensional finite difference scheme, space is discretized into points on a line. The spatial derivative is calculated using a stencil of points that is symmetric about the point where one wants to know the spatial derivative, and extends $n - 1$ points beyond to either side, where n is the order of the expansion. The spatial derivative is calculated from a

weighted sum of the points included in the stencil, where some of the weights are negative. A stencil with $2n - 1$ points in it, in one dimension, corresponds to an n th order expansion. It is possible to expand any order of derivative to any order of expansion. A first derivative, to second order accuracy, given by:

$$D_r^{(2)} = \frac{1}{h} \left(-\frac{1}{2}f_{-1} + \frac{1}{2}f_1 \right) \quad (2.7)$$

Here the f_{-1} and f_1 indicate the function evaluated at the grid point to either side of the 0th grid point, where the derivative is evaluated. Here h is the spacing between grid points. A first derivative, to third order accuracy, is given by:

$$D_r^{(3)} = \frac{1}{h} \left(\frac{1}{12}f_{-2} - \frac{2}{3}f_{-1} + \frac{2}{3}f_1 - \frac{1}{12}f_2 \right) \quad (2.8)$$

Notice how no first order derivative includes the central point in its stencil. In contrast, a second derivative to second order accuracy is given by:

$$D_r'^{(2)} = \frac{1}{h^2} (f_{-1} - 2f_0 + f_1) \quad (2.9)$$

This derivative is symmetric, while the first derivative is antisymmetric.

It is possible to extend these stencils to two and three dimensions. When considering parallelization using OpenMP, issues of synchronization must be considered. When parallelizing over many nodes, the spatial grid gets divided into blocks. At the ends of each block, the boundary cells need information from the neighboring cells to calculate the spatial derivative. For an order n derivative, $n - 1$ boundary cells are synchronized into buffer zones both to the left and to the right at each time step. In our code, this is not necessary, since we have parallelized with OpenMP, which uses shared memory within one node, across several (16) cores.

- **The Discontinuous Galerkin method**

The Discontinuous Galerkin method breaks space into segments called elements. Within each element, the value of the field is represented by the sum of n interpolating polynomials of order n , where n is the order of the element. There are $n + 1$ unevenly spaced nodes in the element, clustered toward the edges. At each node, exactly one of the interpolating polynomials takes on a value of one while the others are zero. An interpolating Lagrange polynomial has a functional form:

$$\ell_i(r) = \prod_{j=1, j \neq i}^n \frac{r - \xi_j}{\xi_i - \xi_j} \quad (2.10)$$

where ξ_i is a location of a node and where r is an arbitrary position [51].

Omitting the details of the derivation of this method, which can be found in Reference [51], the procedure for calculating the spatial derivative in one dimension is to first calculate the Legendre polynomials, rescaled by a factor depending upon their order. $\tilde{P}_n(r) = \frac{P_n(r)}{\sqrt{\gamma_n}}$ where $\gamma_n = \frac{2}{2n+1}$. The following procedure of differentiation and matrix inversion can be used to calculate the derivative matrix for each element, D_r [51].

$$V_{ij} = \tilde{P}_j(r_i) \quad (2.11)$$

$$V_{r,(i,j)} = \frac{d\tilde{P}_j}{dr} \Big|_{r_j} \quad (2.12)$$

$$V^T D_r^T = (V_r)^T \quad (2.13)$$

In practice, we use a custom package, the Template Numerical Toolkit (TNT) library and JAMA, to invert the equation using LU decomposition. Beware! TNT and JAMA are not thread safe, and cannot be used with shared memory parallelization. They result in race conditions, and it was ultimately necessary to rewrite the parallelized portion of the code to avoid the TNT classes.

The Discontinuous Galerkin method helps damp error introduced by discontinuities in

the field, provided they remain at element boundaries. We make use of this in our self-force calculations in the neighborhood of the particle, to be described in Chapter 5.4. The numerical flux is a way of accounting for the discontinuity in the flow between neighboring elements. There are multiple ways of calculating this flux, but in our code, we use a version relevant to linear hyperbolic problems, such as Equation 2.7, which, recall, is specialized to a one-dimensional problem. In this case, $A = S\Lambda S^{-1}$, for some transformation matrix S , where Λ is a diagonal matrix. Let Λ^+ and Λ^- be the positive and negative eigenvalues of Λ , respectively, corresponding to the outgoing and ingoing waves. Then the numerical upwind flux is given by

$$(\hat{n}\dot{F}) = S(\Lambda^+ S^{-1} u^- + \Lambda^- S^{-1} u^+) \quad (2.14)$$

This flux, based upon the state vector interior to (u^-) and exterior to (u^+) the element, at each end of the element, is distributed across the whole element from end to end via the lift matrix [51].

2.2.2 Time evolution

Time evolution in our code is handled by a fourth order low storage Runge Kutta method. Instead of the standard fourth order Runge Kutta method, this method takes five sub-timesteps, but only the most recent sub-timestep needs to be stored.

$$p^{(0)} = u^n k^{(i)} = a_i k^{(i-1)} + \delta t RHS(p^{(i-1)}, t^n + c_i \delta t) p^{(i)} = p^{(i-1)} + b_i K^{(i)} u_h^{n+1} = p^{(5)} \quad (2.15)$$

Here steps two and three are repeated for $i = 1 - 5$, first k , then p , then increase i and repeat. The coefficients a_i , b_i , and c_i are given in Reference [51].

2.3 Wave equation on flat spacetime

Using gaussian initial conditions in ψ and setting the ρ initial conditions to the derivative of that gaussian, I have produced the evolution shown in Figure 2.1. The gaussian marches to the right over a number of time steps, hits the periodic boundary conditions,

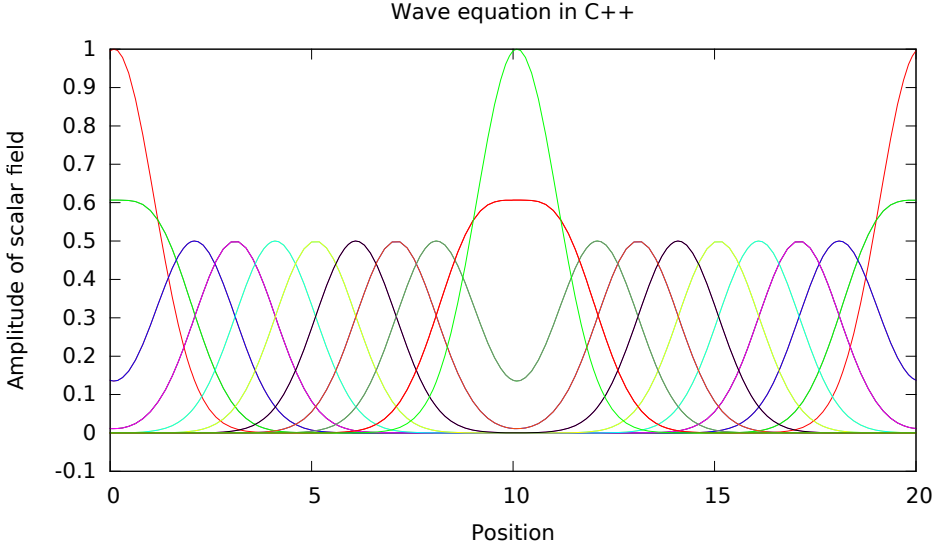


Figure 2.1: Waves evolving over time for gaussian initial conditions

and re-enters the one-dimensional space on the left, eventually returning to its original position. A similar progression can be seen in Figure 2.2 for sinusoidal initial conditions.

The Discontinuous Galerkin method has truncation error that scales as h^{n+1} , where h is the element size and n is the polynomial order of the elements. The L_2 error is defined as the square root of the sum of the squared differences across all space, after one complete cycle of the system. The scaling of the L_2 error with DG order and with element size is shown in Figures 2.3 and 2.4. The scaling matches expectations until roundoff error is hit, where the error stops improving with order or smaller element size. Not shown, this same pattern was seen for the L_0 error, which is the maximum error over all space.

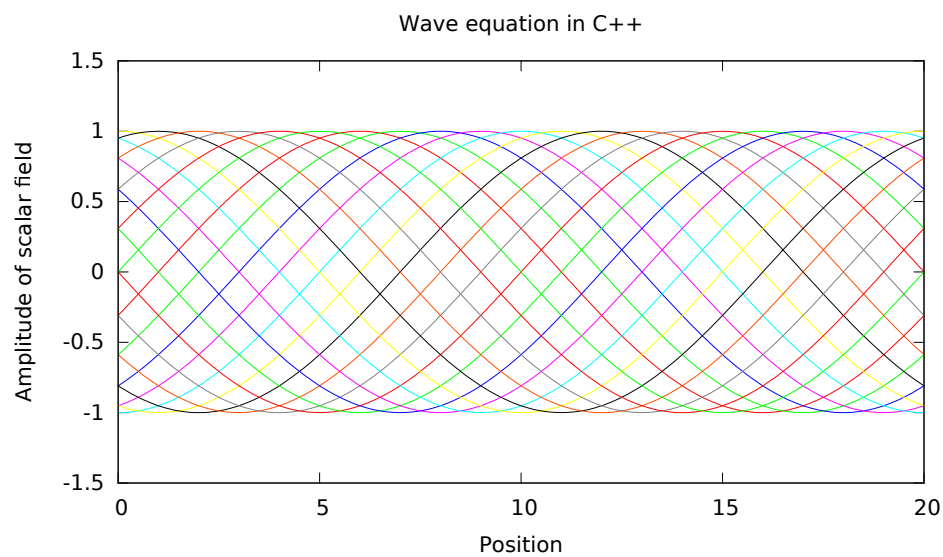


Figure 2.2: Waves evolving over time for sinusoidal initial conditions

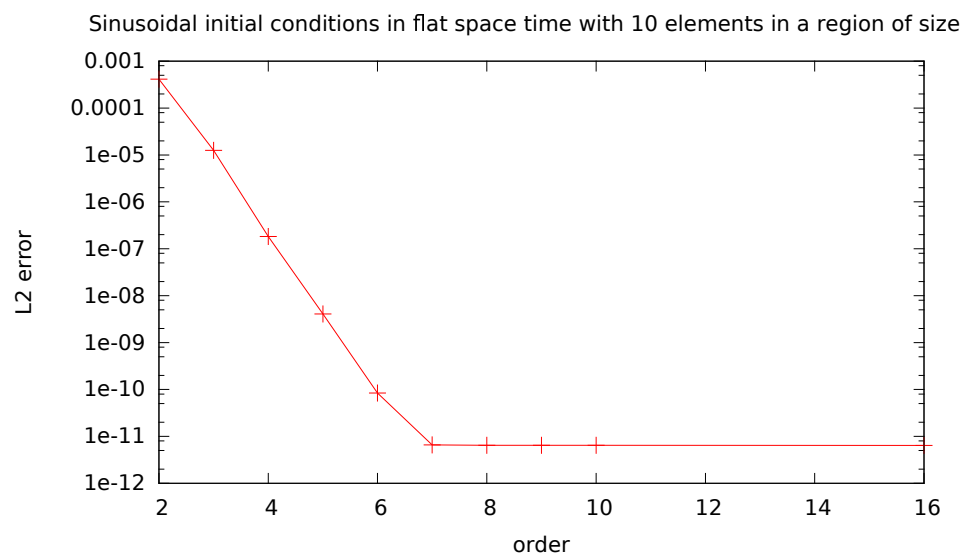


Figure 2.3: L_2 error scaling with DG order for sinusoidal initial conditions

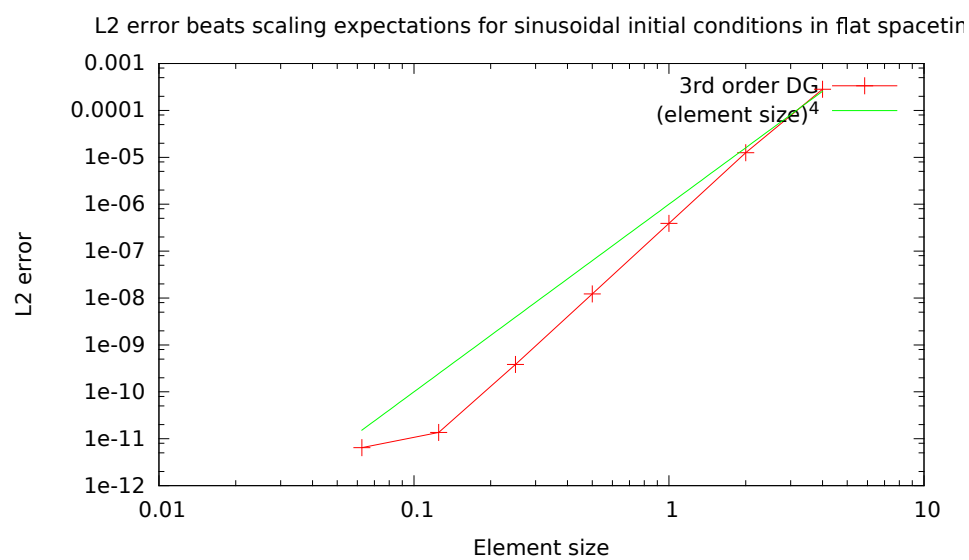


Figure 2.4: L_2 error scaling with element size for sinusoidal initial conditions

Chapter 3

A scalar field on a Schwarzschild background without a source

3.1 Scalar field on Schwarzschild spacetime

Although the final goal in this field is to compute tensor waveforms that can be used as templates for LISA searches, for the purposes of obtaining the desired accuracy, it is important to improve our computational methods. We do this by performing comparison studies using scalar, rather than tensor, self force methods to make the problem more tractable. I have performed the simplest of such comparison studies– I have reimplemented Peter Diener’s Fortran scalar self-force code, with a slightly modified design, in C++. The desired goal was for the results to match to within roundoff error. This was achieved for scalar fields without a source and for scalar fields with point sources on circular orbits (see Chapter 4.2).

3.1.1 Scalar field wave equations

A scalar field is a field that has one one degree of freedom at a given point in space– rather than being a matrix, it has a single value. The scalar wave equation, on a Schwarzschild background, in the absence of a source, is, in its most abstract form, the same as in flat spacetime.

$$\square\Psi = 0 \tag{3.1}$$

The details of the implementation are a little different, to account for the curvature of space. This enters through the metric. For a scalar field, the D’Alembertian can be written

$$\square\Psi = \frac{1}{\sqrt{-g}}\partial_\mu(\sqrt{-g}\partial^\mu\Psi) = 0 \tag{3.2}$$

where g is the determinant of $g^{\mu\nu}$. [56]

- **Multipole moment decomposition**

In our approach, spherical harmonics are used to reduce the three spatial dimensions to a one dimensional problem, in terms of the radius and a sum of an infinite number of discrete spherical harmonic modes, characterized by numbers l and m , where l ranges from 0 to ∞ and m ranges from $-l$ to $+l$ for each l [20]. The field is written as

$$\Psi = \sum_{l,m} \Psi^{lm}(t, r) Y^{lm}(\theta, \phi) \quad (3.3)$$

This separation of variables ansatz can be used to simplify the wave equation in any coordinate system, since the angular coordinates are not transformed in any of the coordinate systems we use. We make use of the identity

$$r^2 \nabla_{\theta, \phi}^2 Y^{lm} = -l(l+1) Y^{lm} \quad (3.4)$$

where $\nabla_{\theta, \phi}^2$ is the angular part of the Laplacian, which has a $\frac{1}{r^2}$ dependence. This introduces a term proportional to $l(l+1)\Psi^{lm}(t, r)$ for each l, m .

- **Tortoise coordinates**

In this code, we use a mixture of tortoise (Eddington-Finkelstein) and hyperboloidal coordinates. Tortoise coordinates have the property that they go to infinity at the horizon (scri minus) and infinity at lightlike infinity (scri plus). It is beneficial to place scri minus at an unreachable distance in coordinate space so that the boundary conditions at the horizon become trivial and there is no leakage of information from the interior of the blackhole to outside the horizon in the process of discretization. It is also beneficial to increase the number of computational elements near the horizon by compactifying the coordinates there. Tortoise coordinates transform only the radial coordinate, leaving the

angular and time coordinates alone. [56]

$$t_* = t \tag{3.5}$$

$$r_* = r + 2GM \ln \left| \frac{r}{2GM} - 1 \right| \tag{3.6}$$

$$\theta_* = \theta \tag{3.7}$$

$$\phi_* = \phi \tag{3.8}$$

We solve the wave equation in tortoise coordinates in one region of the code. I have rederived this equation in Mathematica and verified the form that appears in Peter Diener's Fortran scalar self-force code. The wave equation in tortoise coordinates is

$$\frac{d^2\psi}{dt^2} = \frac{d^2\psi}{dr_*^2} - \frac{1}{r^5} \left(\frac{2M}{r} + (l+1)l \right) \left(1 - \frac{2M}{r} \right) \psi \tag{3.9}$$

r is in Schwarzschild coordinates, r_* is in tortoise coordinates, l is the spherical harmonic l -mode (discussed below), which accounts for the angular dependence, and ψ is a function of tortoise coordinates.

- **Hyperboloidal coordinates**

Hyperboloidal coordinates are necessary; however, because infinities are computationally unreachable. It is clear that space infinitesimally close to the horizon is important, since the curvature of space is strongest there, and it is still causally connected to the exterior region. To make the horizon reachable in a finite number of computational elements, while retaining the property that more computational elements are placed near the horizon than far away, hyperboloidal coordinates are introduced in the region closest to the horizon. In a middle region, tortoise coordinates are used. In the region furthest from the blackhole, hyperboloidal coordinates are used again to place scri plus at a finite number, yet maintaining the property that fewer computational elements are needed far away from the blackhole. Hyperboloidal coordinates are described by the transformation [14]

There are a few key features. The angular coordinates are not transformed. The time coordinate preserves the stationarity of the background metric, and thus the new time variable, τ , must be related to the old time variable, t_* , by an offset dependent only upon r_* , $\tau = t - h(r_*)$. For ingoing waves in the inner region, $t - r_* = \tau - \rho$ and in the outgoing region, $t + r_* = \tau + \rho$ to preserve the structure of the light cone. Bernuzzi, Nagar, and Zenginoglu define $H = \frac{dh}{dr_*}$. They introduce a compactification that depends on a window function Ω [19], such that the tortoise radius gets redefined $r_* = \frac{\rho}{\Omega(\rho)}$, resulting in an expression for the height function H in terms of the hyperboloidal radius, $H(\rho) = 1 - \frac{\Omega^2}{\Omega - \rho\Omega'}$. Their final wave equation, for ingoing waves, is [14]

$$\begin{aligned} \partial_t^2 - \partial_{r_*}^2 = & -(1 - H^2)\partial_\tau^2 \\ & + (1 - H)(-2H\partial_\tau\partial_\rho + (1 - H)\partial_\rho^2 - (\partial_\rho H)(\partial_\tau + \partial_\rho)) \end{aligned} \quad (3.10)$$

I have verified this equation, and derived the outgoing wave equation, in Mathematica.

- **Initial conditions and boundary conditions**

Since there is no source for the scalar field in the C++ code, it must be set to some initial value and allowed to fall into the blackhole or radiate away its energy to infinity. A gaussian initial condition in the time derivative of the scalar field, centered at computational coordinate zero (which was some physical distance outside the black hole horizon), was chosen. Initial conditions and the first timestep are shown in Figures ??.

Boundary conditions were matched automatically by the coordinate transformation between tortoise and hyperboloidal layers. At scri minus and scri plus, the boundary conditions were that the scalar field be set to zero.

3.2 Theoretical expectations

The phase without a source is like the ringdown phase of the system. There are two analytically predicted behaviors that characterize the ringdown phase. After the plunge from the innermost stable circular orbit, quasinormal mode ringing begins. Eventually that

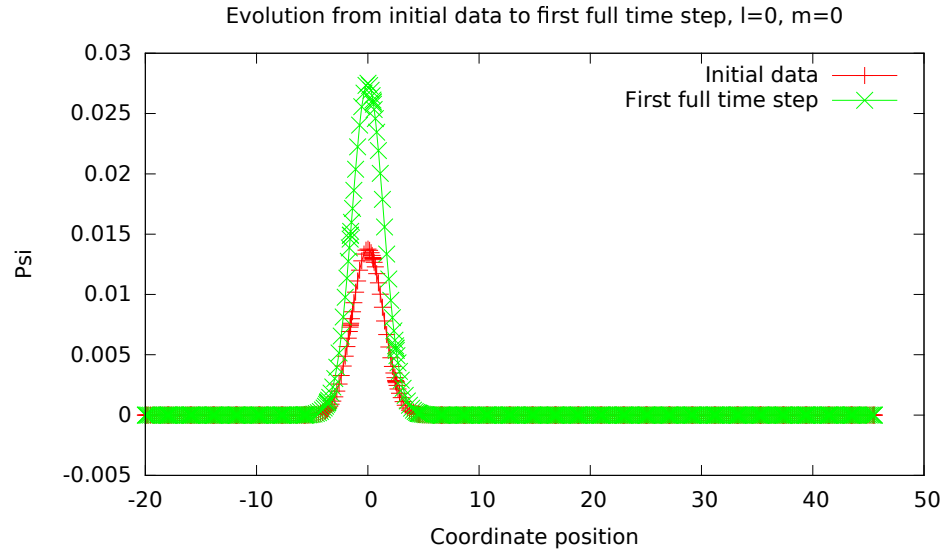


Figure 3.1: Scalar field spatial slice initial condition and first full timestep for $l=0$.

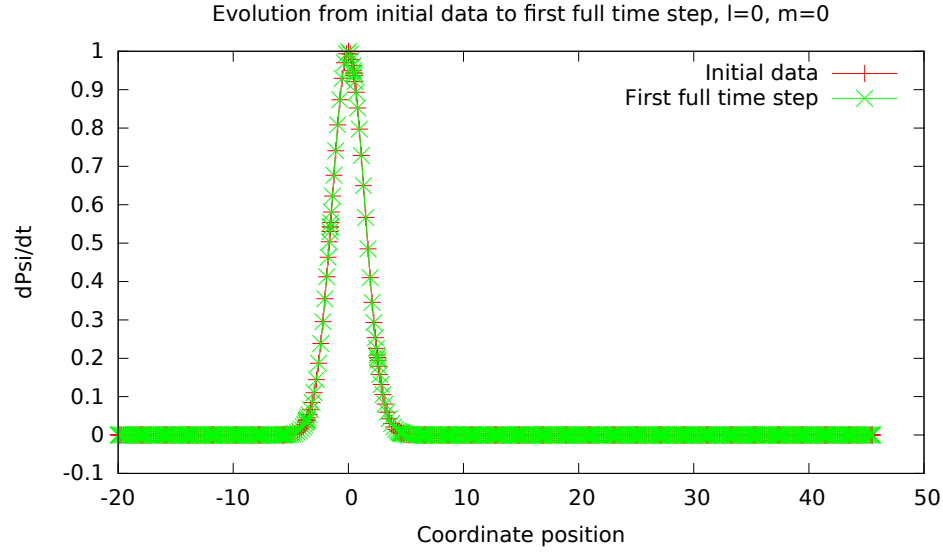


Figure 3.2: Time derivative of the scalar field spatial slice initial condition and first full timestep for $l=0$.

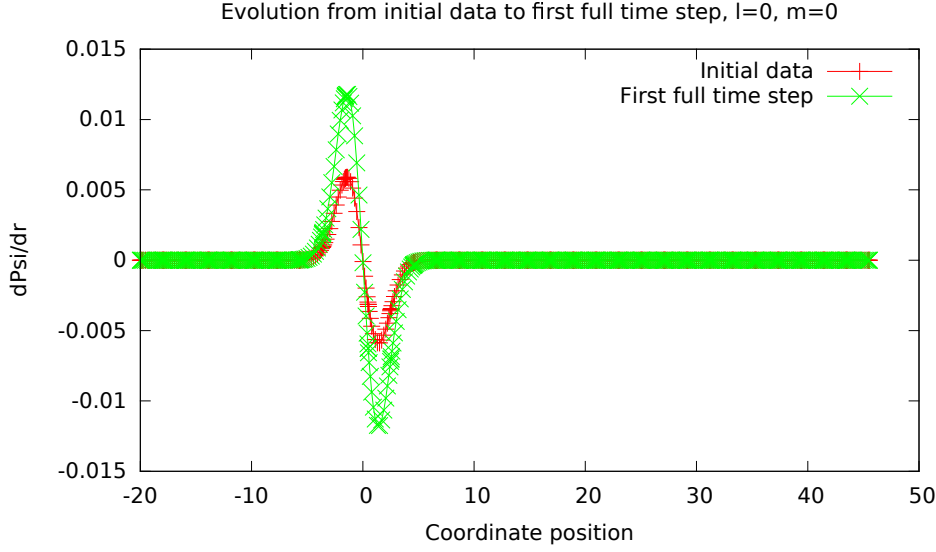


Figure 3.3: Radial derivative of the scalar field spatial slice initial condition and first full timestep for $l=0$.

fades into a long, power law tail.

3.2.1 Quasinormal modes

A field, such as a scalar or tensor field surrounding a blackhole, exhibits quasinormal mode ringing as it relaxes into or away from the blackhole. Hence, in LIGO, the first overtone of the first fundamental quasinormal mode was seen after the merger phase during the ringdown phase in LIGO's first detection [41]. In EMRI's, quasinormal modes are expected to be detected by LISA after the small black hole crosses the large blackhole's horizon, following the plunge from the innermost stable circular orbit. The same set of quasinormal modes is expected for any tensor field perturbed around a blackhole, regardless of why, as long as there is no ongoing source present. The case is very similar with scalar fields, though the spectrum of quasinormal modes is slightly different.

A quasinormal mode decays at a nearly stably frequency and a nearly steady exponential decay rate, with slight changes due to the loss of energy from the system. These rates have been calculated by Reference [5] and made available online. I have used their theoretical expectations for the first overtone at each l and m mode to fit my simulation data in Figures [?] and [?]. Notice that for higher m , the quasinormal mode frequency is

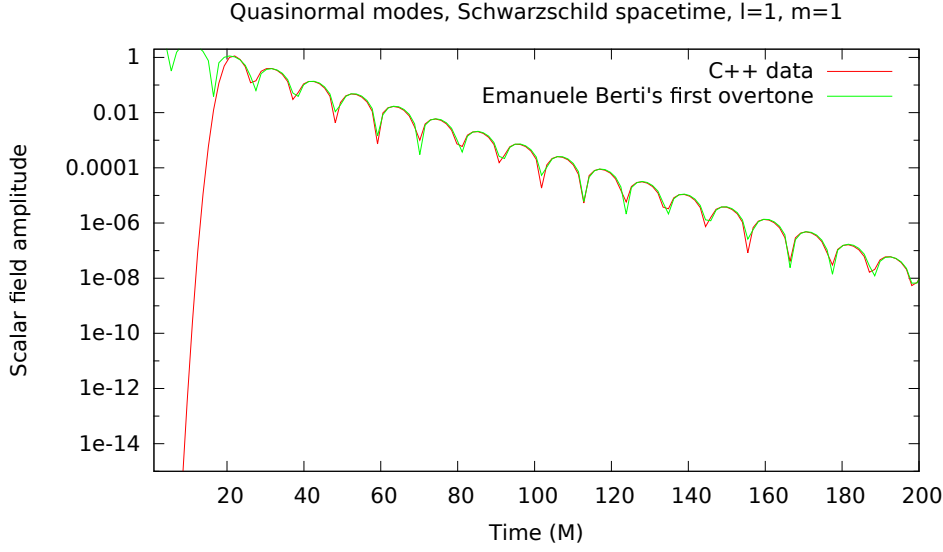


Figure 3.4: Quasinormal mode for $l=1, m=1$

higher and the decay is faster.

3.2.2 Power law tails

After quasinormal mode ringing settles down, power law tails begin. Both are due to backscattering of the waves off the background metric, but they take place in different regimes of time that has elapsed relative to perturbation initial conditions and background blackhole mass. In 1972, Richard Price predicted that the tails would scale as $t^{-(2l+2)}$ or $t^{-(2l+3)}$ depending on initial conditions [1]. In our choice of initial conditions, $t^{-(2l+2)}$ matches best for the choices of l explored. Figure 3.6 shows a mode for which I successfully recovered a power law tail. Figure 3.7 demonstrates that truncation error may dominate at high l , and that it may be necessary to increase the DG order to resolve all l -modes in a simulation.

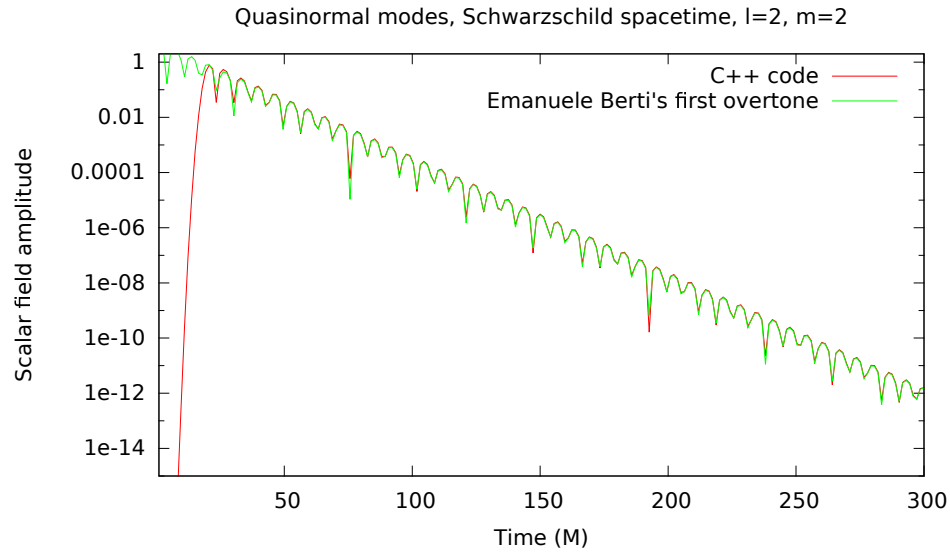


Figure 3.5: Quasinormal mode for $l=2$, $m=2$

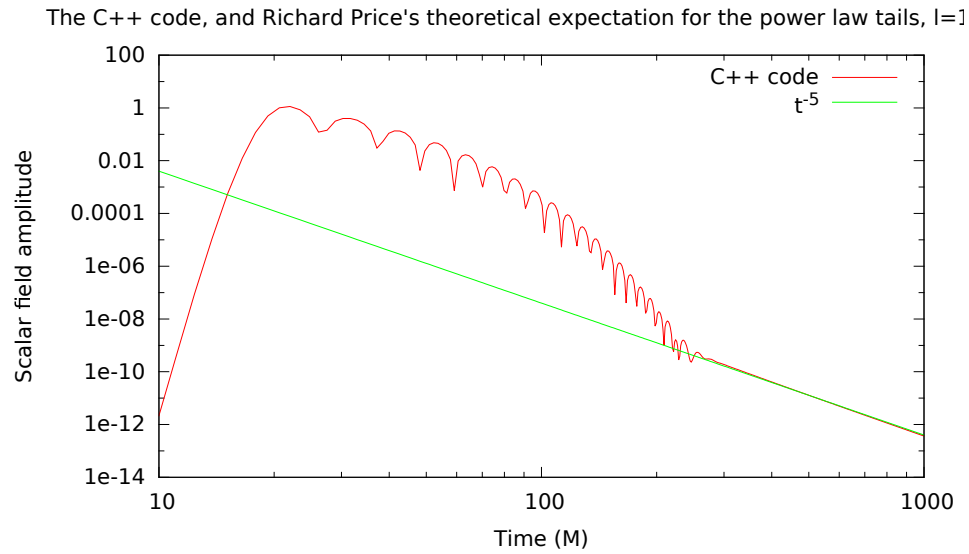


Figure 3.6: Power law tail, $l=1$, $m=1$

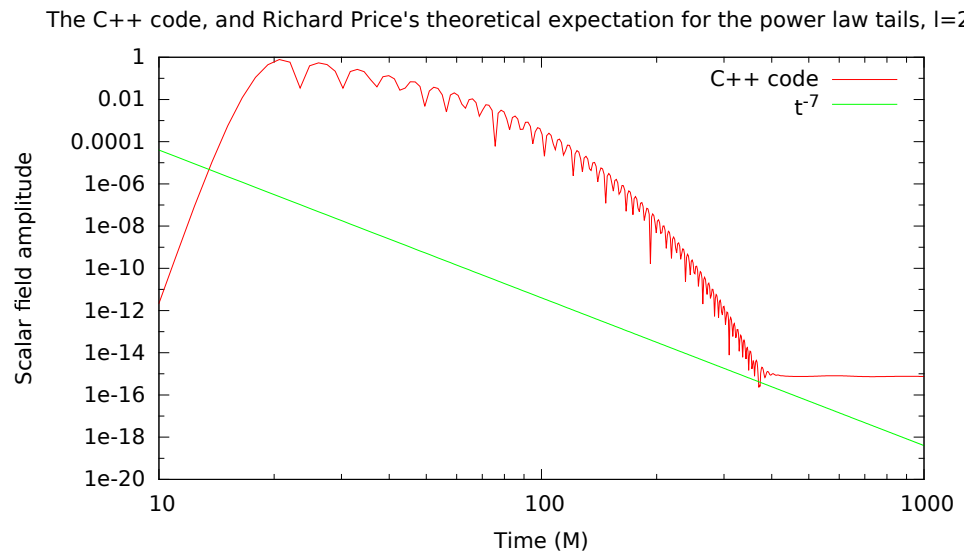


Figure 3.7: Power law tail does not match expectations due to truncation error in DG method, $l=2$, $m=2$

Chapter 4

Circular orbits on a Schwarzschild spacetime

4.1 Self Force

A test particle orbiting a blackhole follows a geodesic, which is the path of extremal proper time. This is described by the geodesic equation,

$$\frac{d^2 x^\mu}{d\tau^2} + \Gamma_{\rho\sigma}^\mu \frac{dx^\rho}{d\tau} \frac{dx^\sigma}{d\tau} = 0 \quad (4.1)$$

where τ is the proper time and $\Gamma_{\rho\sigma}^\mu$ is the Christoffel symbol, given by [57]

$$\Gamma_{\mu\nu}^\sigma = \frac{1}{2} g^{\sigma\rho} (\partial_\mu g_{\nu\rho} + \partial_\nu g_{\rho\mu} - \partial_\rho g_{\mu\nu}) \quad (4.2)$$

However, a blackhole, of any size, is not a test particle. In the limit of an EMRI, the additional force can be treated perturbatively in the mass ratio of the two particles, in the relativistic case. In the scalar case, the self force is simply written as a delta function source to the wave equation dependent upon the particle's position in time [32]

$$\square \Psi^{ret} = -4\pi q \int \delta_4(x, z(\tau')) d\tau' \quad (4.3)$$

In this equation, \square is the D'Alembertian and $z(\tau')$ is the evolving path of the source in spacetime as a function of the particle's proper time. The retarded field Ψ^{ret} , is defined to be the field determined by physics taking place at $t_r = t - \frac{|\vec{r} - \vec{r}'|}{c}$; that is, at some distance away from the particle's path, the physical effects of gravity on the scalar field are retarded by light travel time. In the scalar approximation, the particle acts as a delta function point source, with a charge of q and mass m . That charge may accelerate or evolve with time; see chapter 9.2.3.

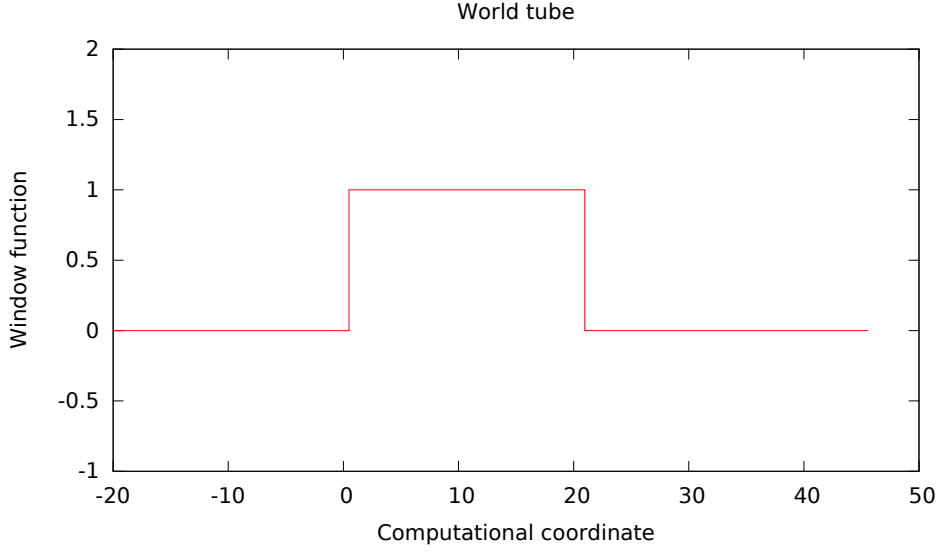


Figure 4.1: Spatial slice of the world tube window function.

The retarded field is singular at the location of the particle due to the delta function source. Singularities are computationally problematic. To regularize this singularity, a regular field is created through the use of an effective source.

$$\Psi^R = \Psi^{ret} - \Psi^S \quad (4.4)$$

$$\square \Psi^R = S_{eff} \quad (4.5)$$

$$S_{eff} = q\delta(x, x_0) - \square(W\Psi^S) \quad (4.6)$$

$$F_\alpha = (\nabla_\alpha \Psi^r)|_{x=x_0} \quad (4.7)$$

The regularized field, Ψ^R , is defined in terms of the retarded field with the singular field, Ψ^S , subtracted. This leads to the definition of an effective source, S_{eff} , that is zero inside the neighborhood of the particle, due to the world tube window function around the particle, shown in Figure 4.1, and that approximates the source outside that region. Outside that region, the regularized field is equal to the retarded field. The self-force can be derived from the final equation given above, F_α is merely a gradient of the field itself [?].

4.1.1 World tube

The world tube window function around the particle carves out a ring around the blackhole in the orbital plane, due to the use of spherical harmonics to increase the dimensionality of space. In my C++ code, the world tube extends throughout the entire tortoise region, ending at the transitions to the hyperboloidal regions. When calculating numerical fluxes at this boundary, it is necessary to account for both the coordinate transformations between either side of the boundary and the transformation between regular and retarded field.

While on a circular orbit, the particle follows a fixed path that prevents it from inspiraling. This does not conserve energy, since energy is radiated away into the blackhole and to infinity by the scalar waves. Clearly, we are artificially inputting energy into the simulation by holding the particle fixed on its orbit. This, in a nutshell, explains the need for scalar (or gravitational) radiation, and for self force in this limit.

4.2 Comparison between C++ and Fortran codes

I've performed extensive comparisons between Peter Diener's Fortran code ??, implementing the same thing, and my C++ code. To roundoff precision, they agree, as evidenced by the near-machine-precision (10^{-15}) levels of agreement in both absolute and relative error that I achieve in Figures 4.2, 4.3, 4.4, and 4.5

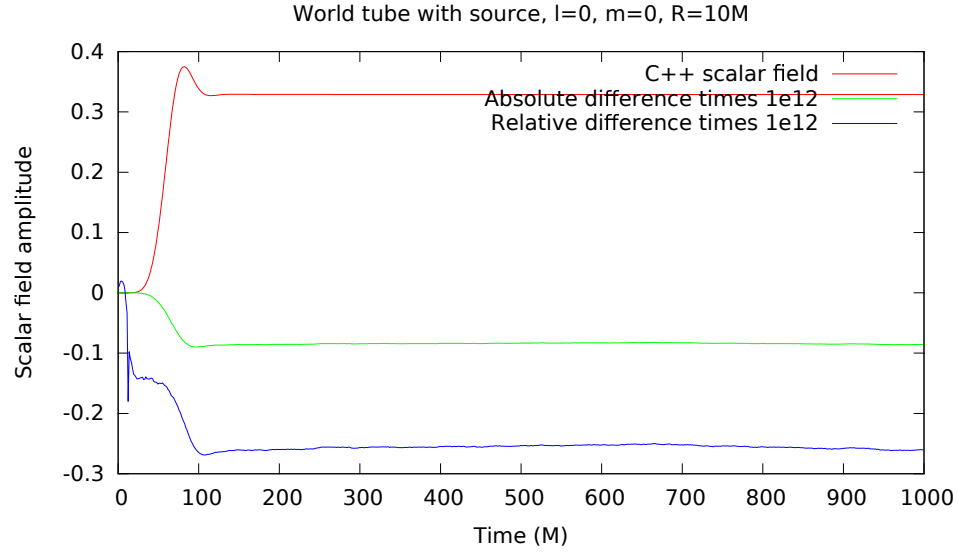


Figure 4.2: Comparison between Fortran and C++ codes for a particle on a circular orbit, $l=0$, $m=0$.

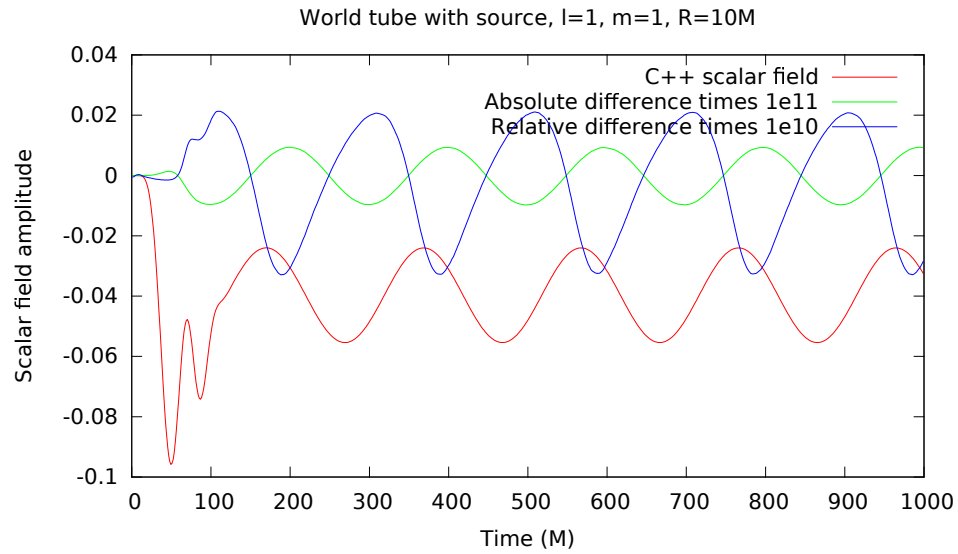


Figure 4.3: Comparison between Fortran and C++ codes for a particle on a circular orbit, $l=1$, $m=1$.

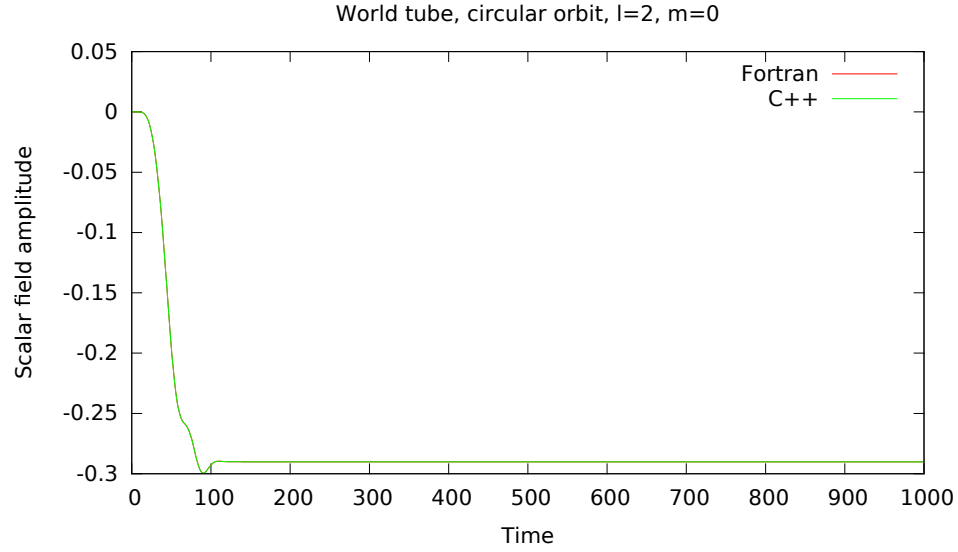


Figure 4.4: Comparison between Fortran and C++ codes for a particle on a circular orbit, $l=2$, $m=0$.

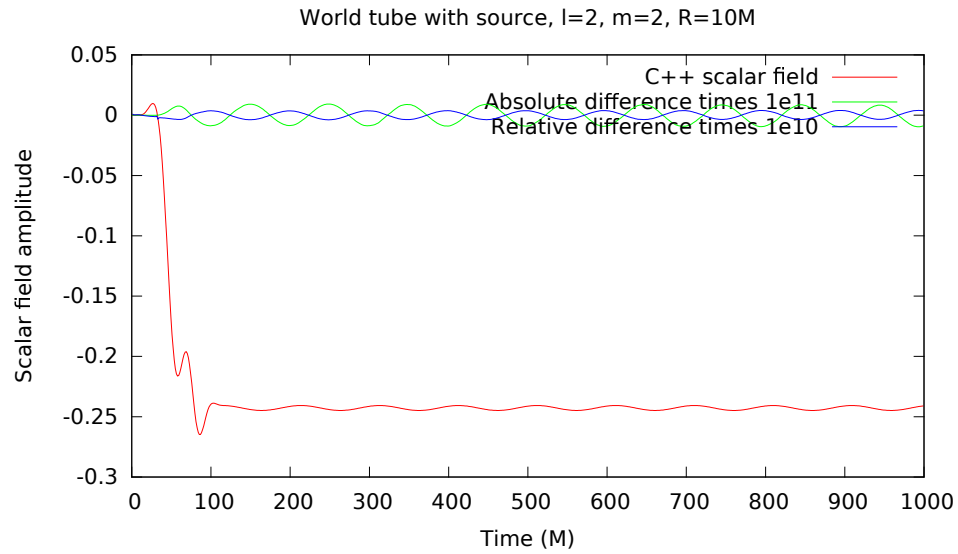


Figure 4.5: Comparison between Fortran and C++ codes for a particle on a circular orbit, $l=2$, $m=2$.

Chapter 5

Elliptical orbits on a Schwarzschild spacetime

For elliptical orbits, there are two primary additional physical or computational effects to consider. One is the need for elliptical orbit parameters, expressed in terms of an eccentricity and a semilatus rectum, determined by an energy and an angular momentum. The second is the addition of a time dependent coordinate transformation region between tortoise layers in the middle of the computational grid, containing the position of the particle for all times. In this section, I describe Peter Diener’s Fortran code, using Niels Warburton’s exact initial conditions for l-modes 0 through 5, and Barry Wardell’s effective source, which I have run to produce elliptical orbit output.

5.1 Orbital parameters (osculating orbits paper)

The orbital parameters of an elliptical orbit in a Schwarzschild spacetime are defined through the following conditions.

$$E^2 = \frac{(p - 2 - 2e)(p - 2 + 2e)}{p(p - 3 - e^2)} \quad (5.1)$$

$$L^2 = \frac{p^2 M^2}{p - 3 - e^2} \quad (5.2)$$

Here, E is the energy and L is the angular momentum. e is the eccentricity and p is the semilatus rectum, which is a dimensionless measure of half the “width” of the elliptical orbit. More clearly, $r_{\text{periastron}} = \frac{pM}{1+e}$ and $r_{\text{apastron}} = \frac{pM}{1-e}$. χ is a parameter that runs from 0 to 2π in one radial cycle (as opposed to ϕ , which runs from 0 to 2π in one angular cycle).

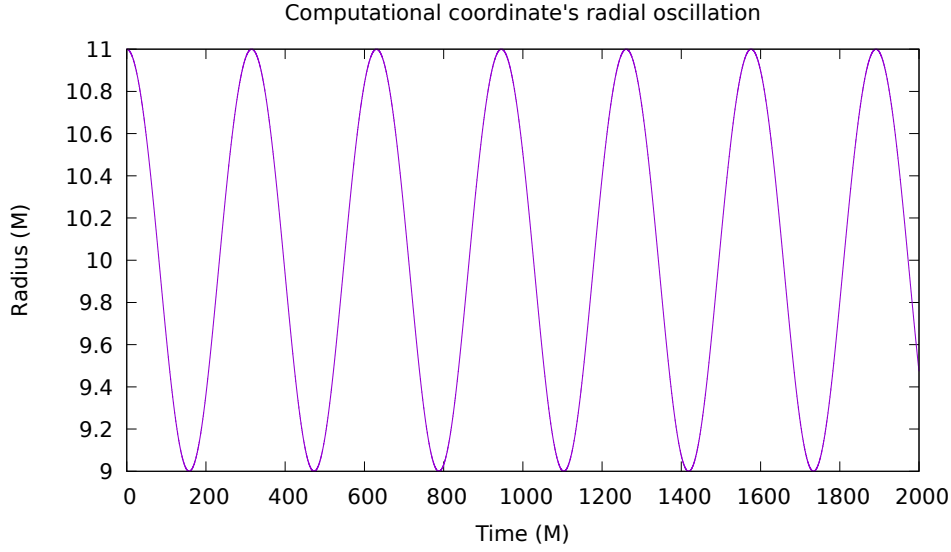


Figure 5.1: Schwarzschild r as a function of time over several orbits.

In terms of these parameters [23],

$$r'(\chi) = \frac{pMe \sin(\chi - w)}{[1 - e \cos(\chi - w)]^2} \quad (5.3)$$

$$\phi'(\chi) = \sqrt{\frac{p}{p - 6 - 2e \cos \nu}} \quad (5.4)$$

$$t'(\chi) = \frac{p^2 M}{(p - 2 - 2e \cos \nu)(1 + e \cos \nu)^2}$$

$$\frac{d\chi}{dt} = \left(\frac{dt}{d\chi}\right)^{-1} \quad (5.5)$$

where $\nu = \chi - w$. For an elliptical orbit, χ and ϕ are evolved using a fourth order Runge Kutta integration using the oscillating orbits framework described in Reference ???. For a self consistent evolving orbit with the backreaction effect of the self-force, see future work in Chapter 9.2.3.

5.2 Time dependent coordinate transformation

In the case of an elliptical orbit, it is necessary to ensure that the particle always remains within the tortoise region, so that the effective source remains valid in the form derived in Reference [2].

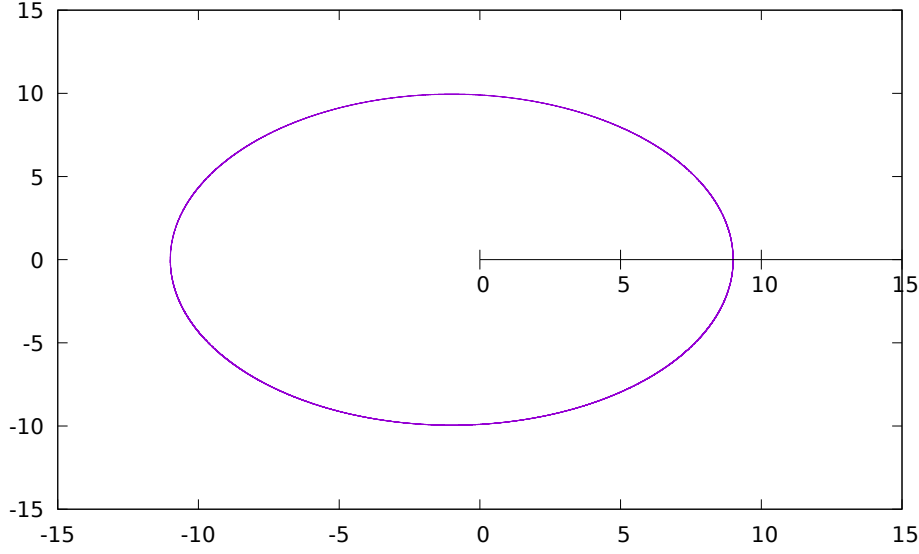


Figure 5.2: With χ as the angle in polar coordinates, the orbit forms an exact ellipse. This is the definition of χ , provided r is in Schwarzschild coordinates. Shown for $p = 9.9$ and $e = 0.1$, DG order 44

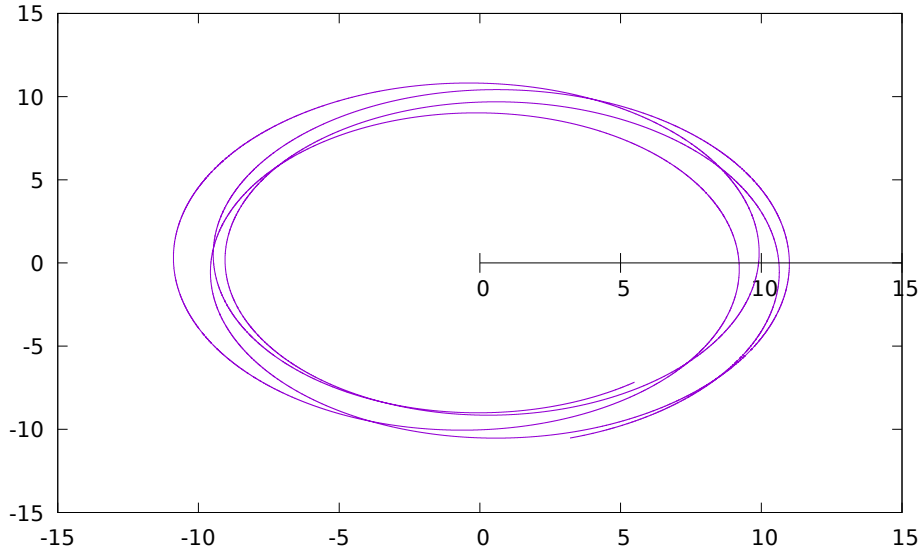


Figure 5.3: The orbit as it physically would exist, using Schwarzschild ϕ as the polar coordinate angle. The orbit precesses but does not inspiral since there is no generic evolution. Shown for $p = 9.9$ and $e = 0.1$, DG order 44

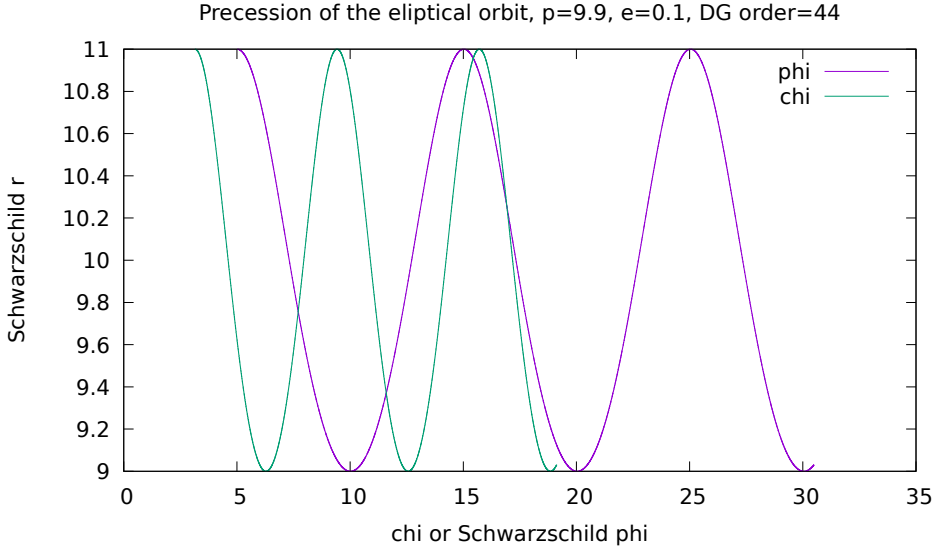


Figure 5.4: Precession of the elliptical orbit is demonstrated due to the inequality in the period of the angular variables χ , which represents the period of the radial oscillations, and ϕ , which represents the period of the angular oscillations. $p = 9.9$, $e = 0.1$, DG order 44.

5.3 Orbbits

5.4 Self Force

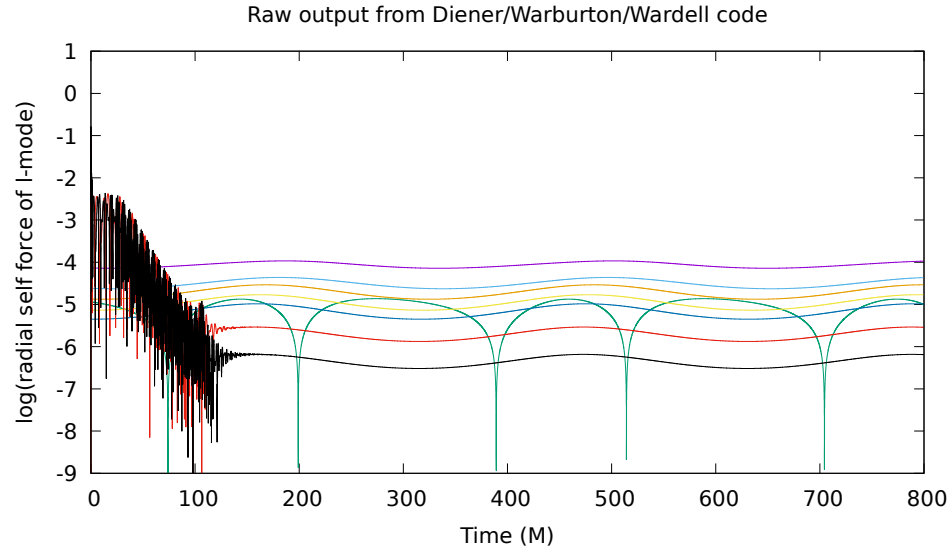


Figure 5.5: Raw output of Diener, Warburton, and Wardell code for DG order 44. Radial self force.

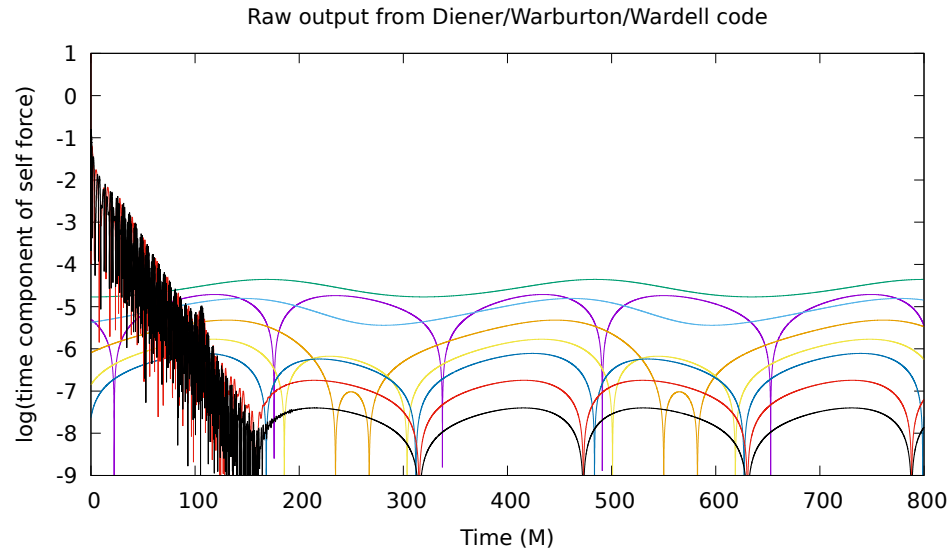


Figure 5.6: Raw output of Diener, Warburton, and Wardell code for DG order 44. Time component of the self force.

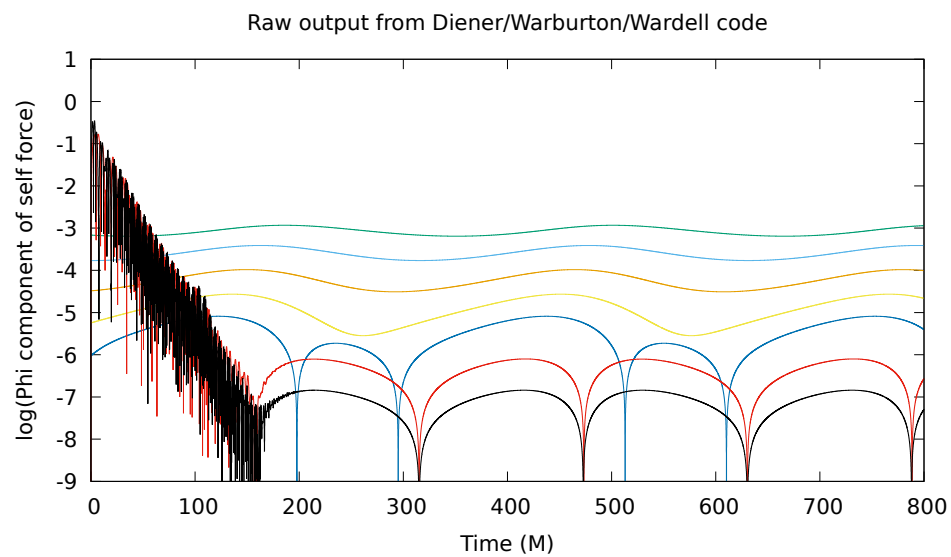


Figure 5.7: Raw output of Diener, Warburton, and Wardell code for DG order 44. Phi component of the self force.

Chapter 6

Extrapolating the self force to infinite Discontinuous Galerkin order

The Discontinuous Galerkin method results in truncation error that scales as h^{N+1} , where h is the element size and N is the order of the interpolating polynomials within the element. [51] The self force is given by the radial derivative of the

Note that it is not always possible to choose three points such that they lie on a converging exponential form, for instance, if they are not monotonic, or if they curve in the wrong direction. In these cases, I say that the “mode failed”, and discard the result for that mode with that starting order for the extrapolation. I use extrapolation starting orders from the set 12, 16, 20, 24, 28, 32, and 36, with additional data at orders 40 and 44 that may be used as points two and three in the extrapolation.

6.0.1 Checking for discontinuities in F_{inf} for each each l-mode

In the median approach, the starting orders that did not “fail” at each time and for each mode are ordered by their F_{inf} values. The median value of F_{inf} is selected, presumably discarding those effected by roundoff and those effected by failure to converge. However, there is no guarantee that it selects those in this regime, since in principle a mode could both be in the roundoff limit and have not converged yet. Yet when this is done, there are no discontinuities in F_{inf} for any of the l-modes when the median approach is used. See mode zero for an example.

time	starting order	finf
632	0	mode failed
632	1	2.40975299617e-05
632	2	2.40975300465e-05
632	3	2.40975300114e-05
632	4	mode failed
632	5	2.40975299291e-05
632	6	2.40975299148e-05

Table 6.1: Manual starting indices and F_{inf} values for t=632, l=2.

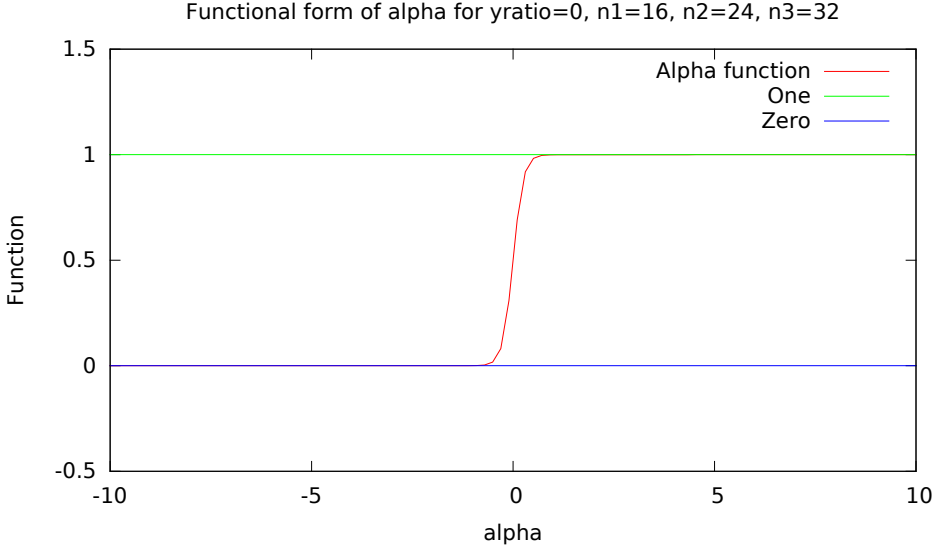


Figure 6.1: $g(\alpha)$

6.0.2 Determining F_{inf} using maximum likelihood fits to subsegments of lines in semilog space

A better motivated approach, is to fit subsegments of lines in semilog space on the DG order convergence plot, and find the most linear, longest linear, region. A fit with the “best” value of the reduced chi squared should be a good approximation to this. The reduced chi squared is the value of the sum of the residuals of the fit squared divided by the number of degrees of freedom, which in this case is the number of points in the fit minus two, since there are two degrees of freedom in a linear fit. The expectation value of the reduced chi squared, in the limit of a large number of degrees of freedom, is one. I loop over starting and ending points of the fit, and over starting orders, and choose the starting order with the best fit line segment in the sense that that line segment has a reduced chi squared closest to one. An example of such an automatically chosen starting index is given in Figure ??, where there is a long exponentially converging region.

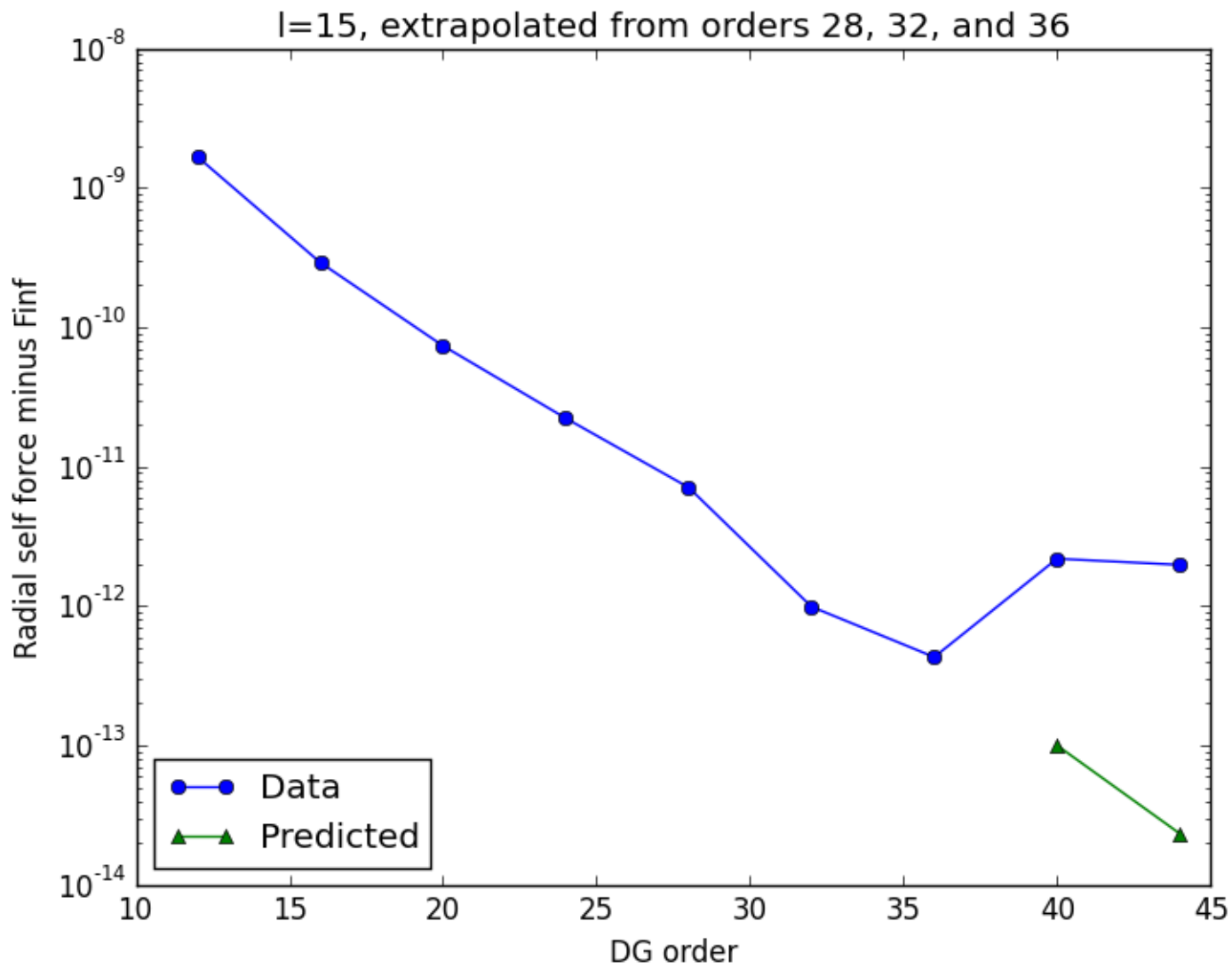


Figure 6.2: DG convergence with order, extrapolated from highlighted points to infinite order along exponential form, which appears as a straight line in the semilog plot.

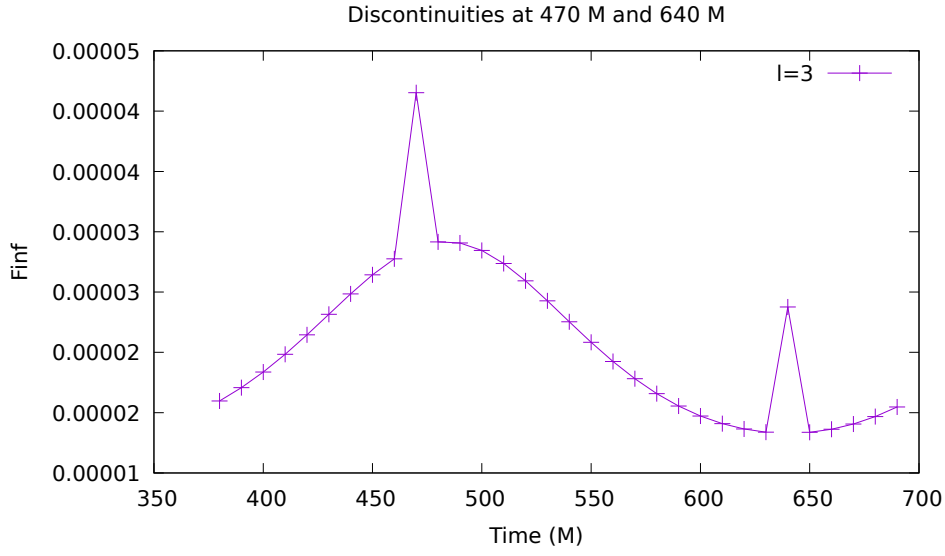


Figure 6.3: Starting order was chosen by iterating from the lowest order to the first order for which the “mode failed”, and choosing the maximum starting order that succeeded. When F_{inf} is evolved over one full orbital cycle, some l-modes show discontinuities at some times. $l=3$

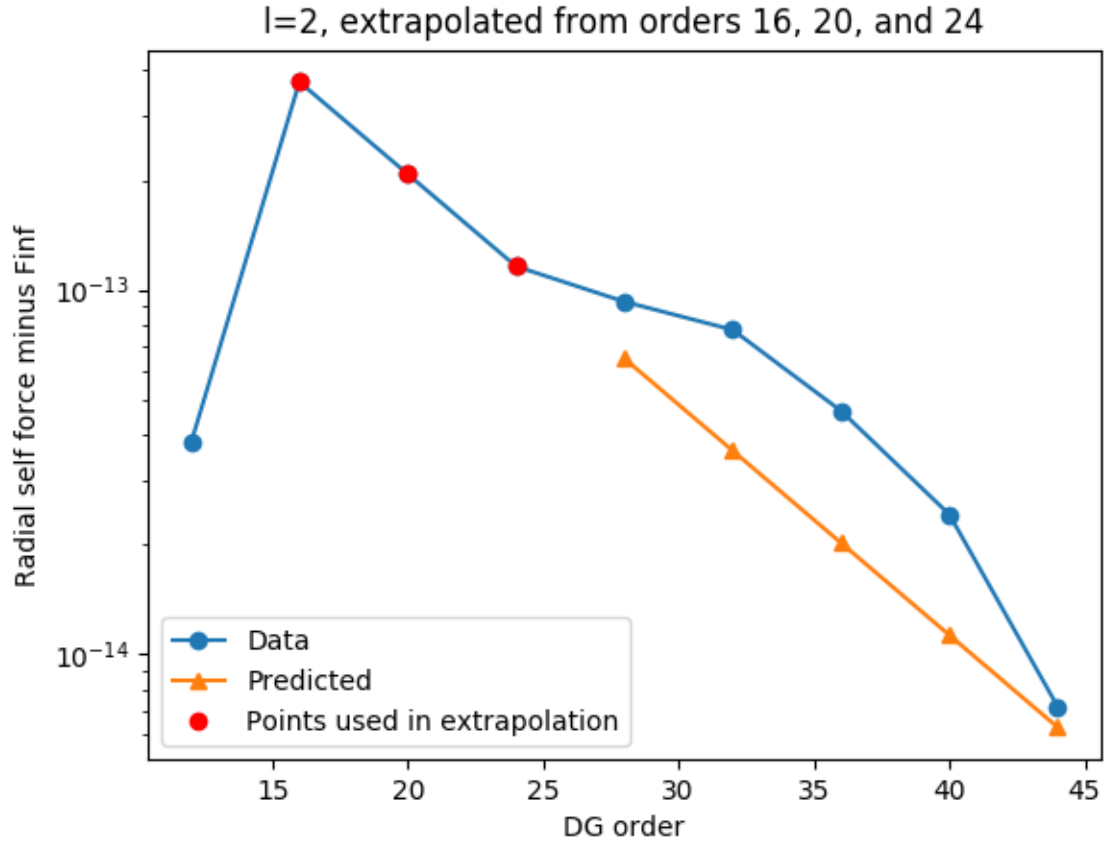


Figure 6.4: Fluctuation in one of the points chosen in the extrapolation, due to roundoff or truncation error, causes the extrapolation to predict a value of F_{inf} that is subtly wrong, leading to curvature in the semilog plot after F_{inf} subtraction. $t=632$, $l=2$, $i=1$

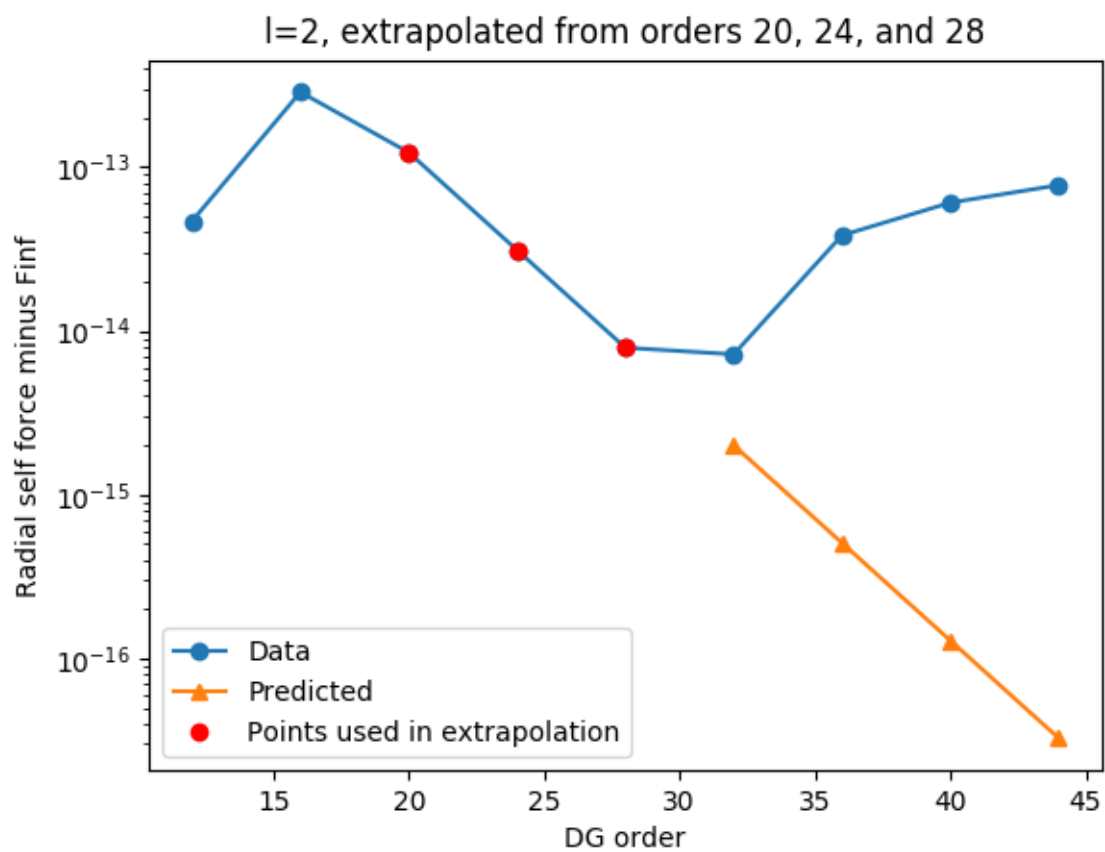


Figure 6.5: Roundoff error is visible at high DG orders. $t=632$, $l=2$, $i=2$

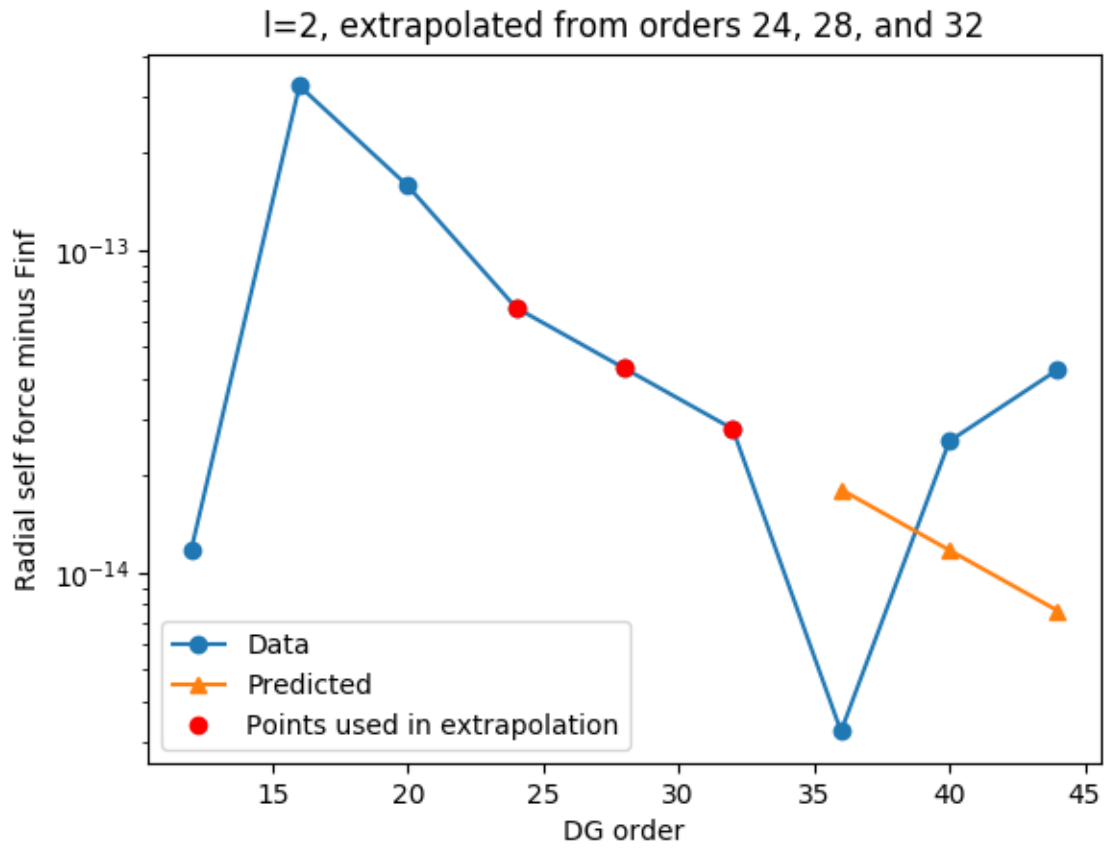


Figure 6.6: The incorrect value of F_{inf} has been chosen due to roundoff error, perhaps due to finite precision in the root finding algorithm, leading to a negative values, that show as a “V” in the semilog plot. $t=632$, $l=3$, $i=3$

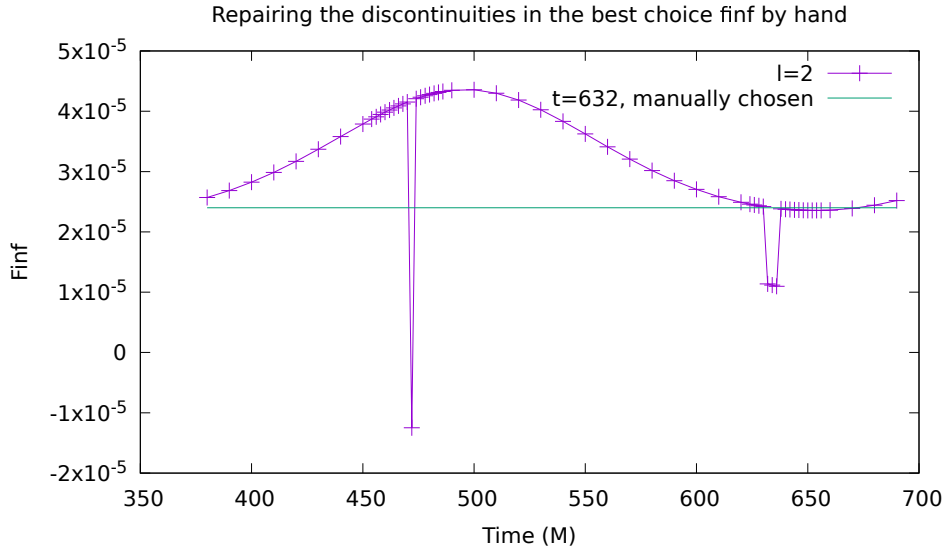


Figure 6.7: Manual correction for the discontinuities in the $l=2$ mode, using the manually determined F_{inf} data from Table 6.1.

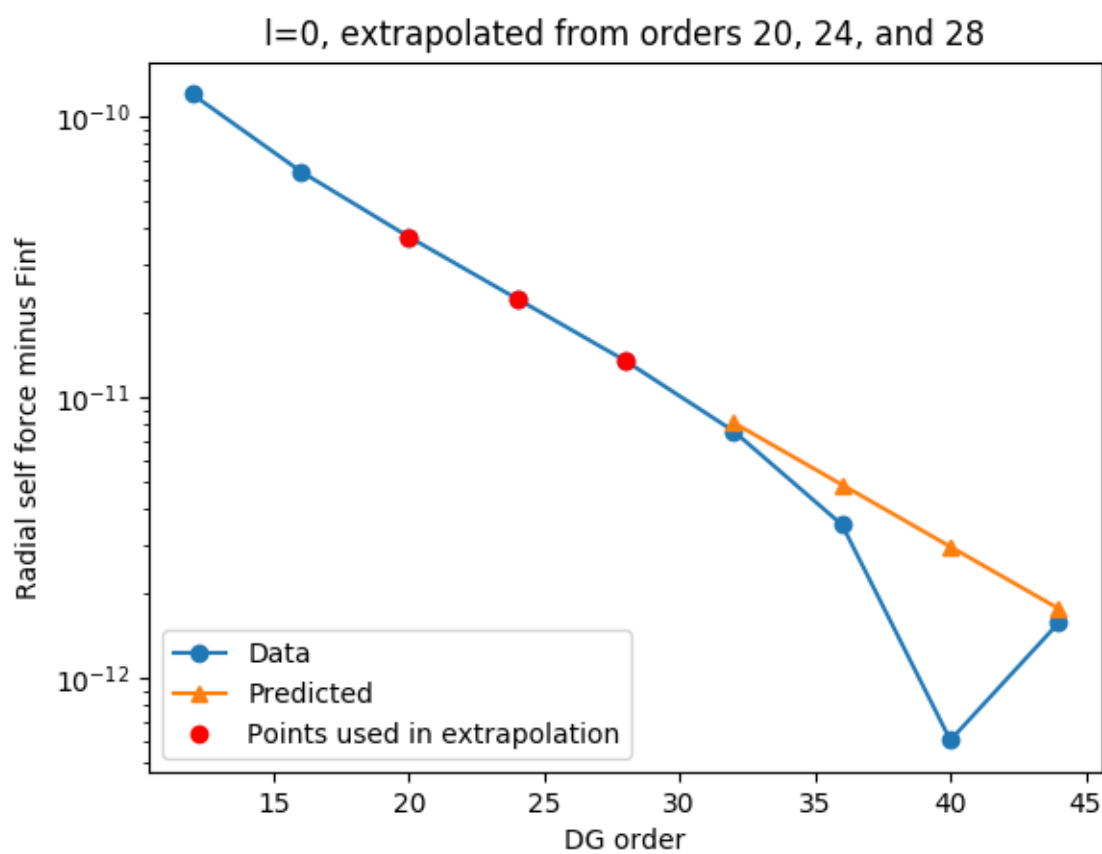


Figure 6.9: $l=0$ mode with line-segment fit-chosen starting order produces convergence plot with long exponentially converging region

Chapter 7

Extrapolating the mode-summed self-force to include contributions from an infinite number of spherical harmonic modes

INCLUDE CITATION AND FUNCTIONAL FORM, FUNCTIONAL FORM OF MODE SUM

$$F_r(l) = \frac{a}{(2l-1)(2l+3)} + \frac{b}{(2l-3)(2l-1)(2l+3)(2l+5)} \\ + \frac{c}{(2l-5)(2l-3)(2l-1)(2l+3)(2l+5)(2l+7)} + \dots \quad (7.1)$$

$$\sum_n^{\infty} F_r(l) = \frac{an}{4n^2-1} + \frac{bn}{3(9-40n^2+16n^4)} \\ + \frac{cn}{5(2n-5)(2n-3)(2n-1)(2n+1)(2n+3)(2n+5)} + \dots \quad (7.2)$$

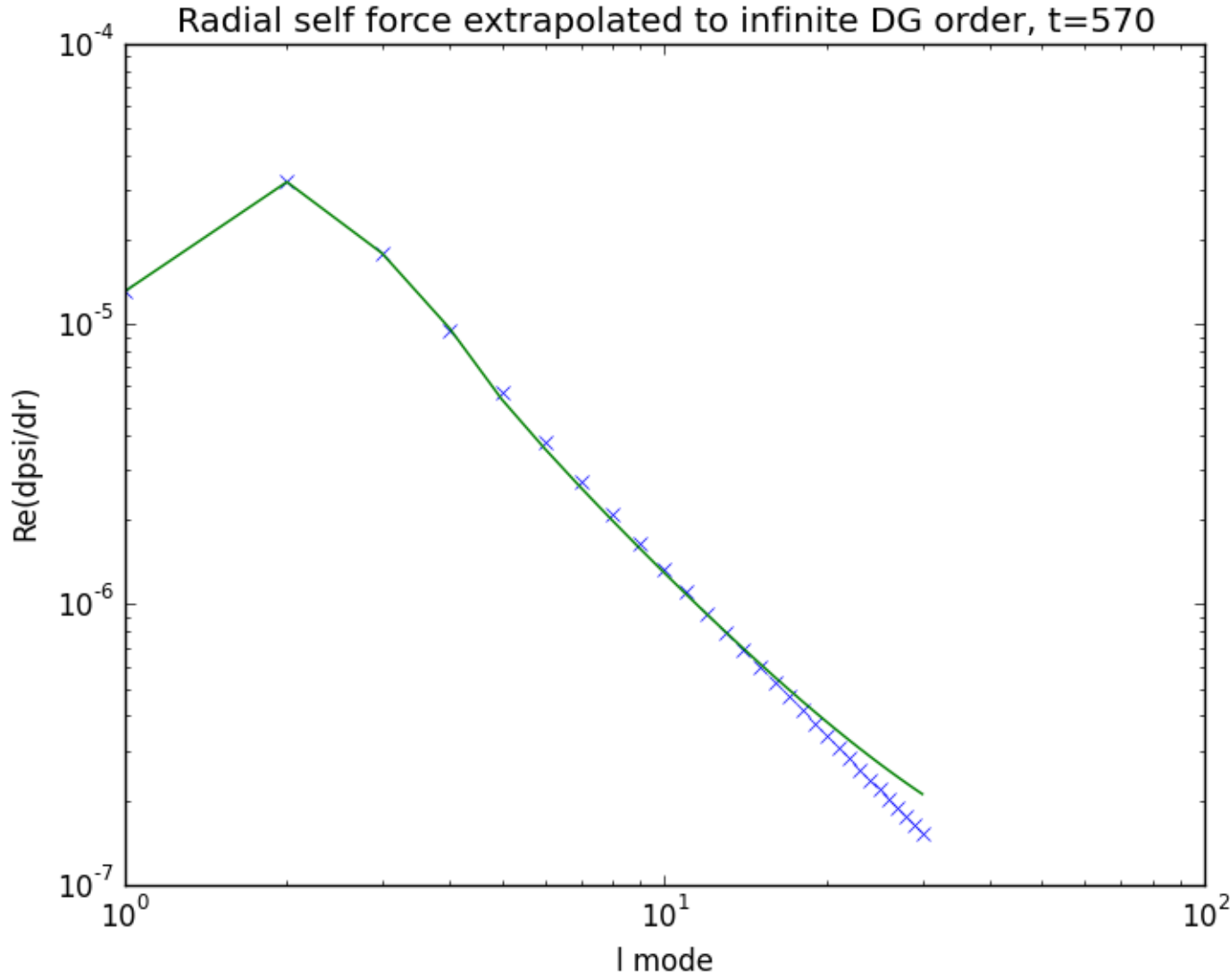


Figure 7.1: Three term fit of l -mode vs F_{inf} . Note how the fit is bad at high l . There are an infinite number of additional terms that can be added to the fit to account for this deviation. However, it is also fundamentally difficult to fit an exponentially converging function. See Chapter 8.1.

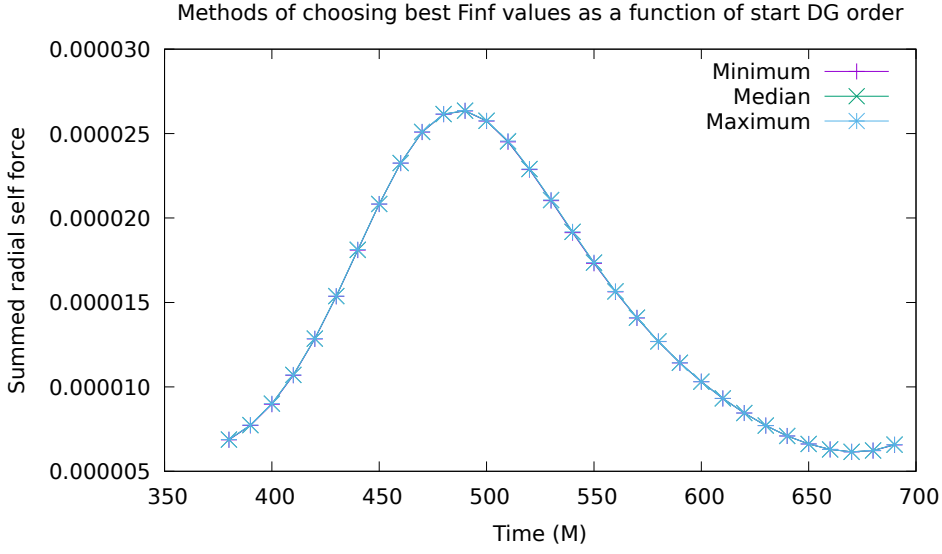


Figure 7.2: This is the actual summed, doubly extrapolated, radial self force, measured in three different ways as described in the three figures above.

take standard deviation of surface plot as well as average.

7.0.1 Fractional errors

7.0.2 Structure of the error compared to the evolution in time

Total radial self force, using DG error extrapolation per l-mode, $t=635$

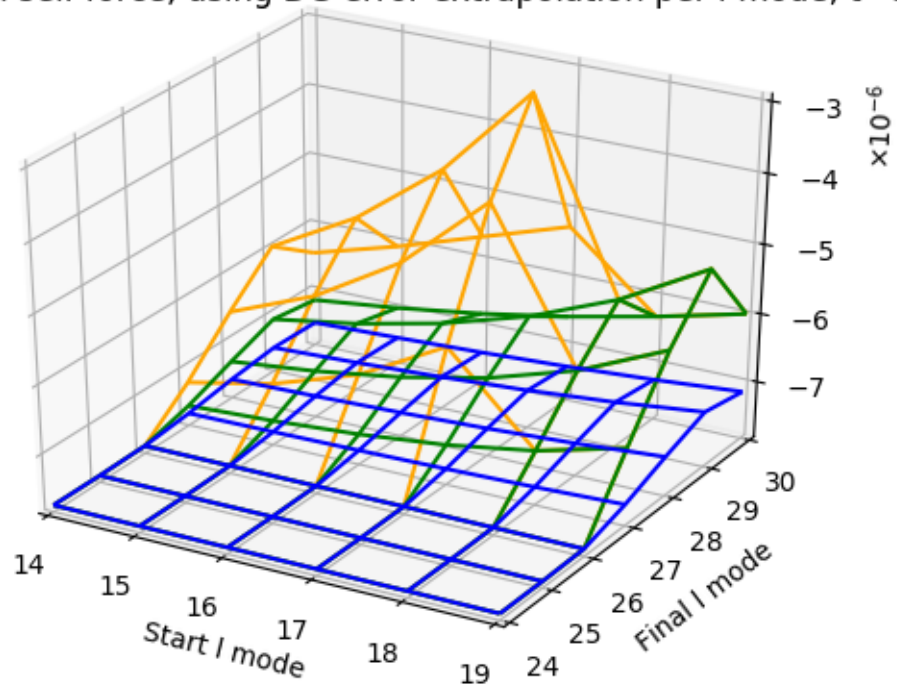


Figure 7.3: $t=635$, 2, 3, and 4 term fits over a broad range of l_{\min} and l_{\max} values. Note the roundoff noise at high l_{\max} . Aphelion, where this effect is worst.

Total radial self force, using DG error extrapolation per l-mode, t=635

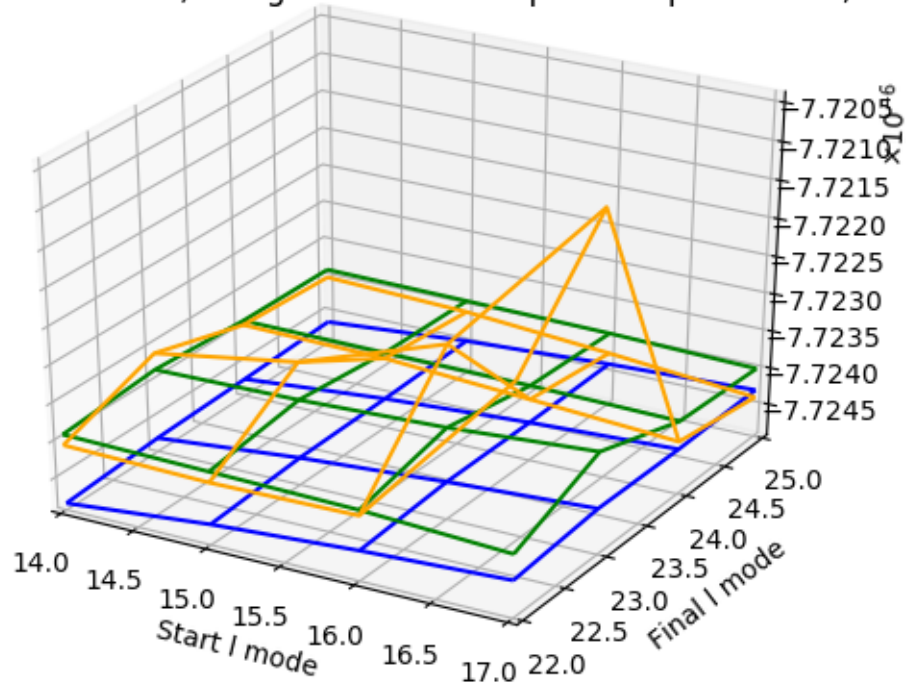


Figure 7.4: t=635, 2, 3, and 4 term fits over a small range of lmin and lmax. This is the actual range used to estimate the total self force. Aphelion, where the roundoff noise is worst. Note that there is not a large difference between two and three terms, and that four terms is less smooth a surface, suggesting that it is more subject to round off noise. Three terms is preferred.

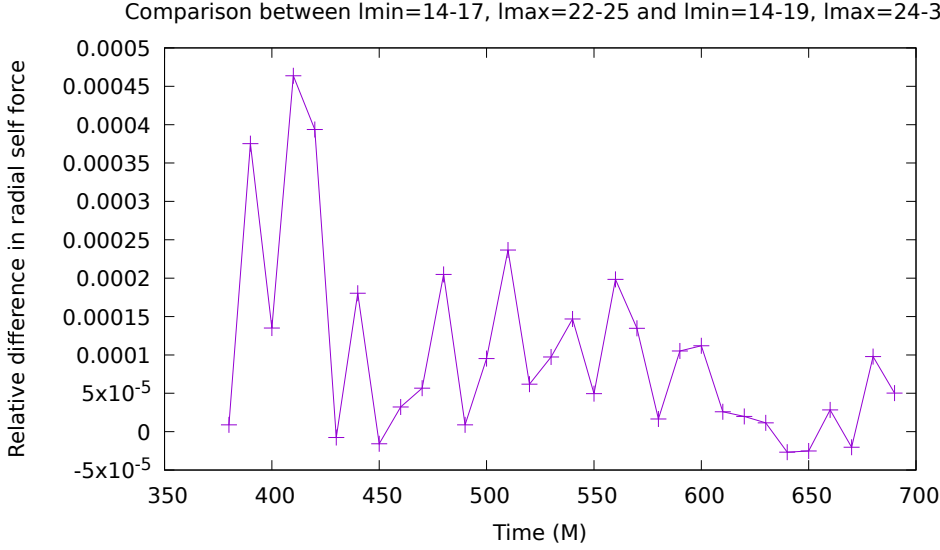


Figure 7.5: This is the relative difference between the total radial self force measured in two different ways. In both cases, the self force was extrapolated to infinite order at every l -mode at every possible DG starting order. The infinite DG order self forces over the various starting orders were sorted, eliminating NaNs. The median was chosen for each l -mode. Then the self force as a function of l -mode was fit to its three term form, and the sum was summed from zero to l_{\max} , then extrapolated from $l_{\max} + 1$ to infinity using an analytic form determined using Mathematica. All possible choices with l_{\min} between 14 and 17 and l_{\max} between 22 and 25 were averaged to obtain the total radial self force as a function of time. Similarly, all possible choices with l_{\min} between 14 and 19 and l_{\max} between 24 and 30 were averaged to obtain the total radial self force as a function of time. This plot shows the relative difference. I believe the smaller range is in the denominator.

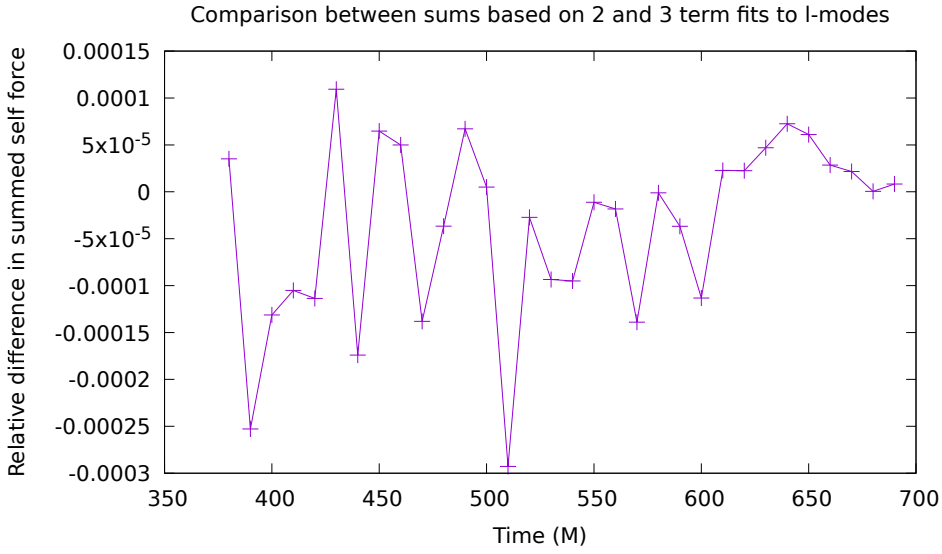


Figure 7.6: This figure was produced in the same manner as the previous figure, averaging over the smaller range, only it is a comparison between including either two or three terms in the l-mode fit. I believe the three term fit is in the denominator of the relative difference.

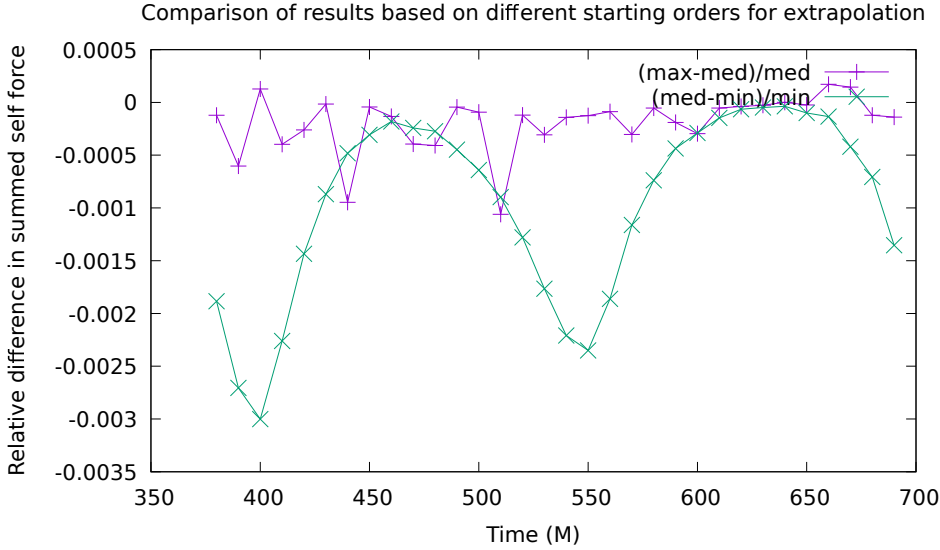


Figure 7.7: This figure was produced in a similar manner to the first figure, only instead of using the median, it is a comparison between using the median, the maximum, and the minimum. The purple line is the relative difference between the maximum and the median, which is subject to roundoff error due to the potential for the maximum to contain roundoff error. The green line is the relative difference between the median and the minimum, which is subject to effects due to failure to converge. I suspect the median is the best compromise between these two effects, rejecting outliers in both directions, though it is a simplistic approach to doing so, and does not guarantee success. It is possible to have a starting order that has not converged and is also in the roundoff regime, for example. A better guarantee of success, though not a certain one, would be to do a fit over part of the error convergence plot to determine exponentiality, by fitting a line in semilog scale. However, this seems unnecessarily complex at this time.

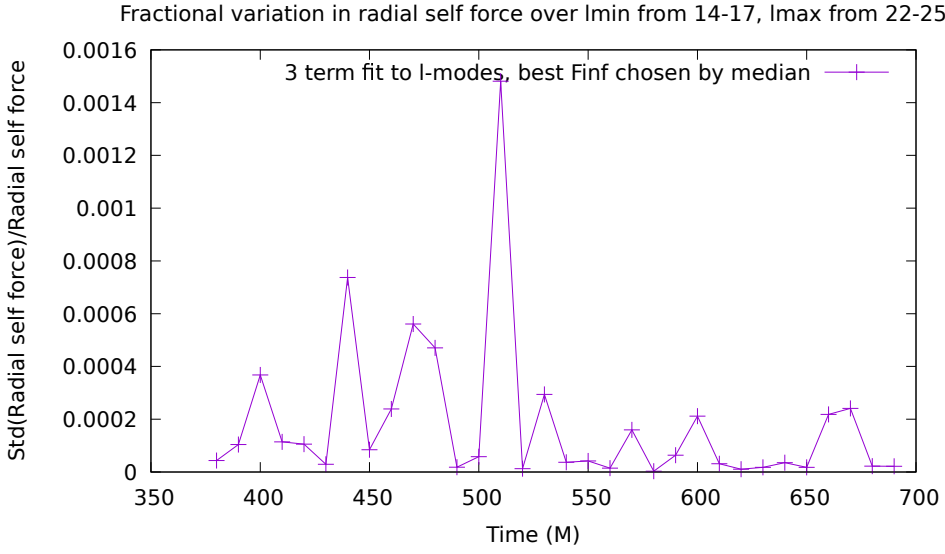


Figure 7.8: 3 term, median method

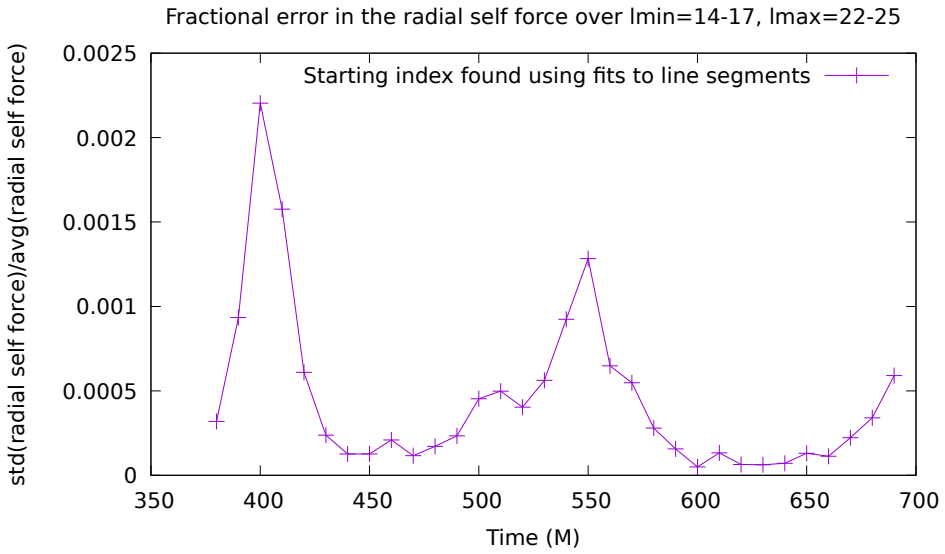


Figure 7.9: 3 term, fit method

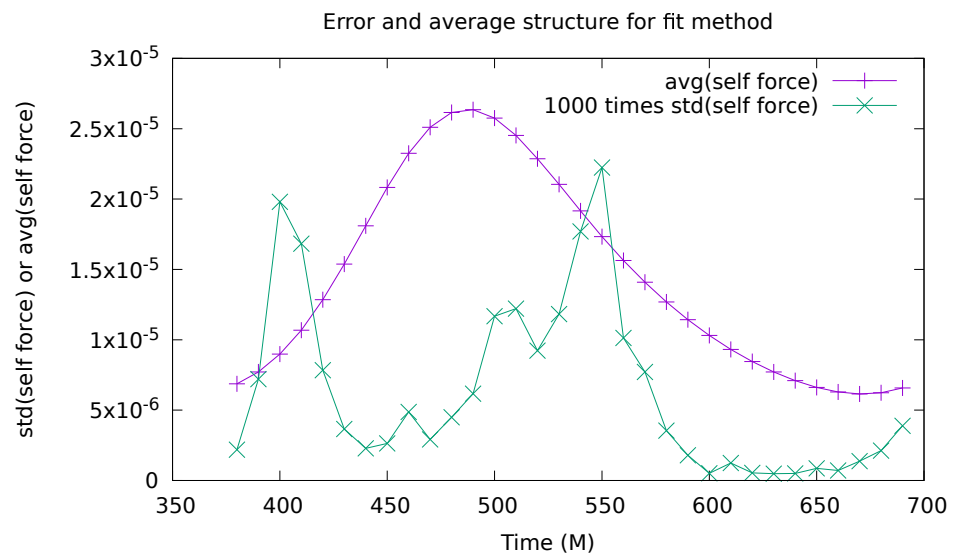


Figure 7.10: The structure of the absolute error in comparison to the evolution in time for the fit method

Chapter 8

Improving mode fits via a power law scaled weight factor in χ^2 sum

8.0.1 Relative error as a function of mode

We can understand why it is so hard to produce good fits by examining the relative error between different fitting techniques as a function of mode. Look at the relative error between the fit method and the median method. One would hope that absolute error decreases with l , such that the infinite series would be convergent. Since the self force over l scales as a power law that goes as l^{-2} to the first order, I suggest a weight that scales as l^{-2} . A weighted fit is of the form

$$\chi^2 = \sum \frac{(f(x_i) - y_i)^2}{\sigma_i} \quad (8.1)$$

where σ_i is a weight related to the “error” or “uncertainty”, in this case the truncation or roundoff error depending which regime the mode is in. Absolute values of weights don’t matter unless the reduced χ^2 is used to select the best fit.

Absolute error increases as l .

8.1 TODO

He also wants convergence plots of the fit data versus the median data for some bad times. I also want a plot that shows the raw data before the subtraction of the offset for some time. Modify code to use saved raw data.

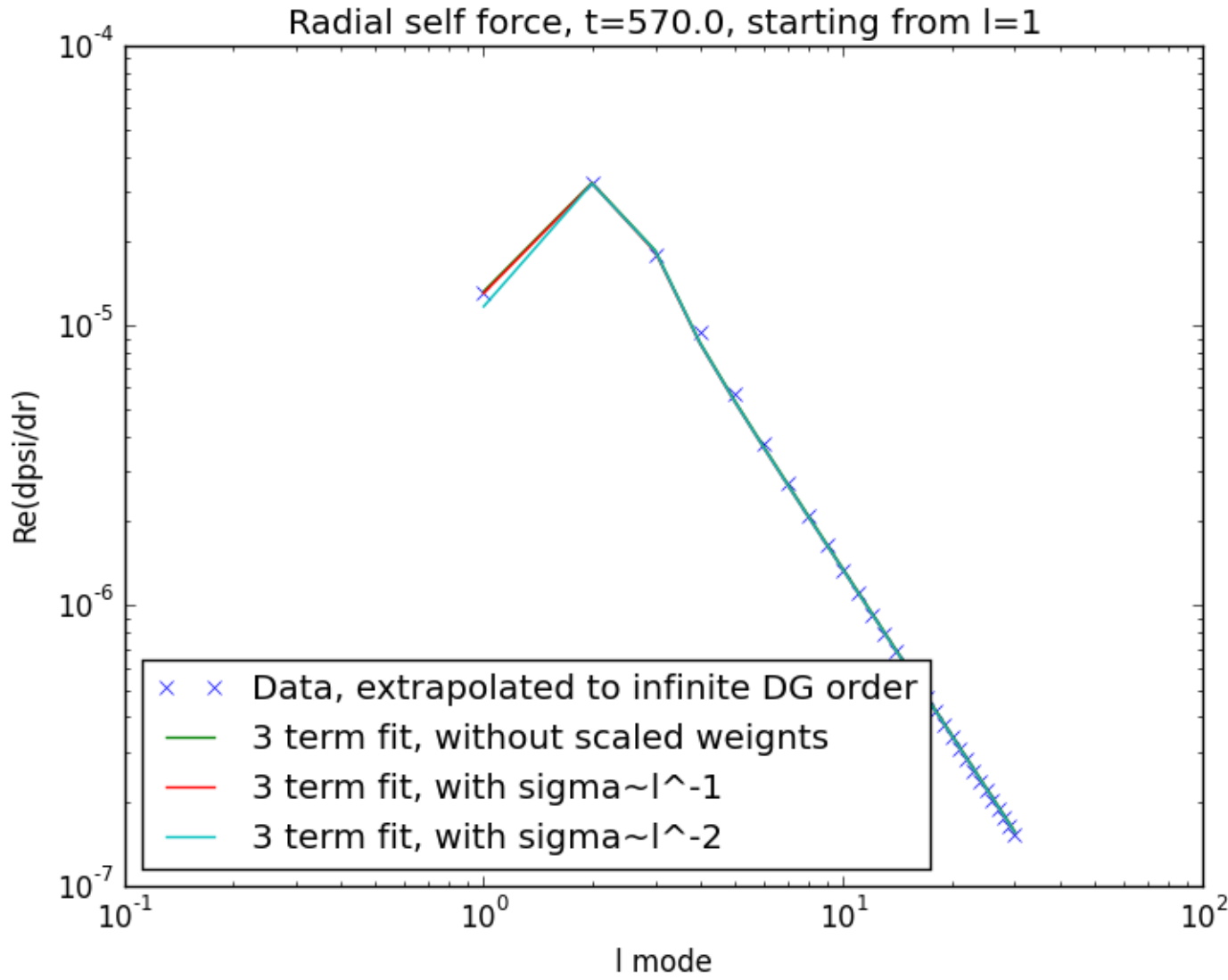


Figure 8.1: $t=570$, $l=1$, three term fit with two different power law scales for weights in comparison to unscaled weights ($\sigma = 1$).

Variation of total radial self force with start and end points of fit

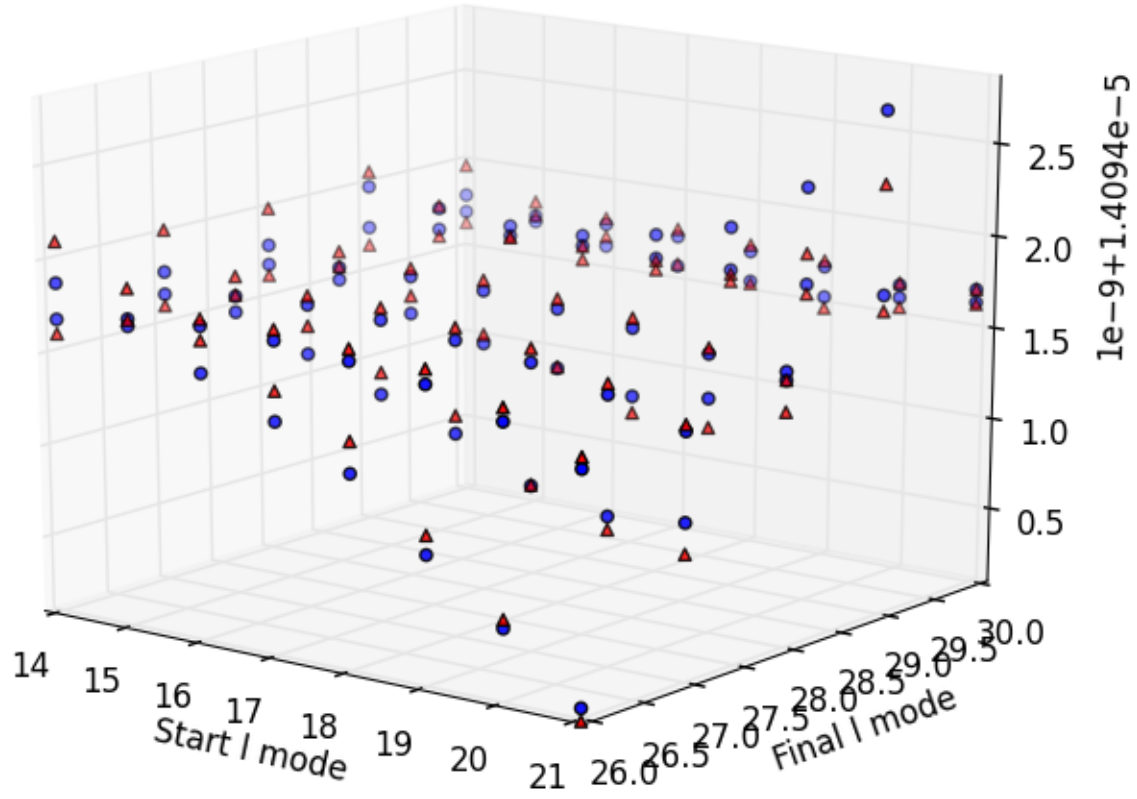


Figure 8.2: The difference between the triangles and the circles shows that the difference in the total radial self force between the presence of a $\sigma \sim l^{-2}$ weight and no weight is unimportant compared to the difference in the total radial self force between various start and end points of the l-mode fit.

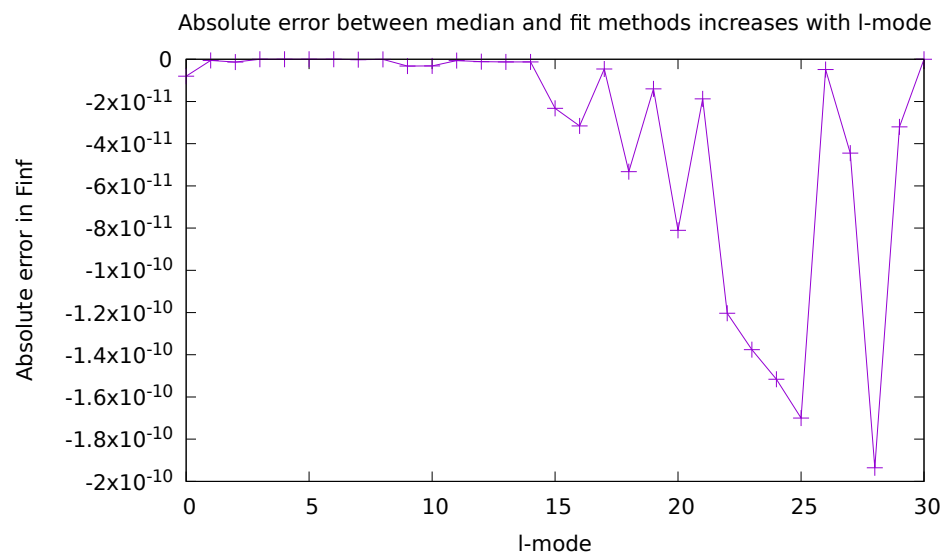


Figure 8.3: Absolute error between fit and median techniques increases with l-mode, explaining why the difference between weight and no weight fit techniques is unimportant.

Chapter 9

Future work: generic orbits via the osculating orbits framework

9.1 plans for the future

going to test Peter Diener's generic orbits and help him develop them further.

$$(\square - \xi R)\Psi^{ret} = -4\pi q \int \delta_4(x, z(\tau')) d\tau' \quad (9.1)$$

$$ma^\alpha = q(g_{(0)}^{\alpha\beta} + u^\alpha u^\beta)\Psi_{,\beta}^R \quad (9.2)$$

$$\frac{dm}{d\tau} = -qu^\alpha \Psi_{,\alpha}^R \quad (9.3)$$

R is the Ricci scalar (0 in Schwarzschild spacetime) and ξ is the coupling to curvature. The first equation gives the scalar wave equation in curved spacetime, with a source. The second equation gives the back-reaction due to acceleration of the particle. Here, Ψ^R is the regularized field. The third equation governs the self-consistent evolution of the mass of the particle. [32]

9.2 Generic orbits

9.2.1 Geodesic evolution

9.2.2 Osculating orbits

9.2.3 methods

effective source osculating orbits time dependent coordinate transformation world tube already implemented with accelerated orbits though I have not run these. future work: make self consistent evolution work.

References

- [1] Price, Richard H. (1972). Nonspherical Perturbations of Relativistic Gravitational Collapse. I Scalar and Gravitational Perturbations. *Phys. Rev. D* 5, 10.
- [2] Miller, Jeremy; Wardell, Barry; Pound, Adam. (2016). Second-order perturbation theory: the problem of infinite mode coupling. *arXiv:1608.0783v1*.
- [3] Heffernan, Anna. (2012). The Self-Force Problem: Local Behavior of the Detweiler-Witing Singular Field. University College Dublin. *arXiv:1403.6177v1*.
- [4] Yang, Huan; Zimmerman, Aaron; Zenginoglu, Anil; Zhang, Fan; Berti, Emanuele; Chen, Yanbei. (2013). Quasinormal modes of nearly extremal Kerr spacetimes: spectrum bifurcation and power-law ringdown. *arXiv:1307.8086v1*.
- [5] Berti, Emanuele; Cardoso, Vitor; Starinets, Andrei O. Quasinormal modes of black holes and black branes. *arXiv:0905.2975v2*
- [6] Philipp, Dennis; Perlick, Volker. (2015). On analytic solutions of wave equations in regular coordinate systems on Schwarzschild background. *arXiv:1503.08101v1*
- [7] Diaz-Rivera, Luz Maria; Messaritaki, Eirini; Whiting, Bernard F.; Detweiler, Steven. (2004). Scalar field self-force effects on orbits about a Schwarzschild black hole. *arXiv:gr-qc/0410011v1*.
- [8] Diener, Peter; Vega, Ian; Wardell, Barry; Detweiler, Steven. Self-consistent orbital evolution of a particle around a Schwarzschild black hole. *arXiv:1112.4821v3*.
- [9] Dirac, P. A. M. (1938). Classical theory of radiating electrons. *Royal Society Publishing*.
- [10] Amaro-Seoane, Pau; Gair, Jonathon R.; Pound, Adam; Hughes, Scott A.; Sopuerta, Carlos F. (2014). Research Update on Extreme-Mass-Ratio Inspirals. *arXiv:1410.0958v1*.
- [11] Gair, Jonathan R.; Porter, Edward K. (2012). Observing extreme-mass-ratio inspirals with eLISA/NGO. *arXiv:1210.8066v1*
- [12] Gralla, Samuel E.; Harte, Abraham I.; Wald, Robert M. (2009). A Rigorous Derivation of Electromagnetic Self-force. *arXiv:0905.2391v2*.
- [13] Heffernan, Anna; Ottewil, Adrian; Wardell, Barry; (2013). High-order expansions of the Detweiler-Whiting singular field in Schwarzschild spacetime. *arXiv:1204.0794v4*.
- [14] Bernuzzi, Sebastiano; Nagar, Alessandro; Zenginoglu, Anil. (2011). Binary black hole coalescence in the large-mass-ratio limit: the hyperboloidal layer method and waveforms at null infinity. *arXiv:1107.5402v2*.
- [15] Danzmann, Karsten. (2017). LISA Laser Interferometer Space Antenna: A proposal in response to the ESA call for L3 mission concepts.

- [16] Babak, Stanislav. (2017). Science with the space-based interferometer LISA. V: Extreme mass-ratio inspirals. *arXiv:1703.09722v1*.
- [17] Miller, Jeremy; Wardell, Barry; Pound, Adam. (2016). Second-order perturbation theory: the problem of infinite mode coupling. *arXiv:1608.06783v1*.
- [18] Mino, Yasushi; Sasaki, Misao; Tanaka, Takahiro. (1996). Gravitational Radiation Reaction to a Particle Motion. *arXiv:gr-qc/9606018v1*.
- [19] Yunes, Nicolas; Wofgang, Tichy; Owen, Benjamin J.; Briigmann, Bernd. (2006). Binary black hole initial data from matched asymptotic expansions. *arXiv:gr-qc/0503011v3*.
- [20] Poisson, Eric; Pound, Adam; Vega, Ian. (2011). The Motion of Point Particles in Curved Spacetime. *arXiv:1102.0529v3*.
- [21] Pound, Adam. (2012). Second-order gravitational self-force. *arXiv:1201.5089v2*.
- [22] Pound, Adam. (2017). Nonlinear gravitational self-force: second-order equation of motion. *arXiv:1703.02836v1*.
- [23] Pound, Adam; Poisson, Eric. (2008). Osculating orbits in Schwarzschild spacetime, with an application to extreme mass-ratio inspirals. *Phys. Rev. D* 77, 044013.
- [24] Quinn, Theodore, C. (2000). Axiomatic approach to radiation reaction of scalar point particles in curved spacetime. *arXiv:gr-qc/0005030v1*.
- [25] Quinn, Theodore C.; Wald, Robert M. An Axiomatic approach to electromagnetic and gravitational radiation reaction of particles in curved spacetime. *arXiv:gr-qc/9610053v1*.
- [26] Field, Scott E.; Hesthaven, Jan S.; Lau, Stephen R. Discontinuous Galerkin method for computing gravitational waveforms from extreme mass ratio binaries. *arXiv:0902.1287v2*.
- [27] Zenginoglu, Anil; Khanna, Gaurav. (2011). Null infinity waveforms from extreme-mass-ratio inspirals in Kerr spacetime. *arXiv:1108.1816v2*.
- [28] Vega, Ian; Diener, Peter; Tichy, Wolfgang; Detweiler, Steven. (2009). Self-force with (3+1) codes: a primer for numerical relativists. *arXiv:0908.2138v1*.
- [29] Vega, Ian; Wardell, Barry; Diener, Peter. (2011). Effective source approach to self-force calculations. *arXiv:1101.2925v1*.
- [30] Vega, Ian; Wardell, Barry; Diener, Peter; Cupp, Samuel; Haas, Roland. (2013). Scalar self-force for eccentric orbits around a Schwarzschild black hole. *arXiv:1307.3476v2*.
- [31] Vega, Ian; Wardell, Barry; Diener, Peter; Cupp, Samuel; Hass, Roland. (2013). Scalar self-force for eccentric orbits around a Schwarzschild black hole. *arXiv:1307.3476v2*.

- [32] Wardell, Barry. (2015). Self-Force: Computational Strategies. *arXiv:1501.07322v3*.
- [33] Wardell, Barry; Vega, Ian; Thornburg, Jonathan; Diener, Peter. (2012). Generic effective source for scalar self-force calculations. *arXiv:1112.6355v3*.
- [34] LIGO Virgo Collaboration. (2016). Observation of Gravitational Waves from a Binary Black Hole Merger. *Phys. Rev. Lett.* 116, 061102.
- [35] LIGO Virgo Collaboration. (2016). GW151226: Observation of Gravitational Waves from a 22-Solar-Mass Binary Black Hole Coalescence. *Phys. Rev. Lett.* 116, 241103.
- [36] LIGO Virgo Collaboration. (2017). GW120104: Observation of a 50-Solar-Mass Binary Black Hole Coalescence at Redshift 0.2. *Phys. Rev. Lett.* 118, 221101.
- [37] LIGO Virgo Collaboration. (2016). Observing Gravitational-wave Transient GW150914 with Minimal Assumptions. *Phys. Rev. D* 93, 122004.
- [38] LIGO Virgo Collaboration. (2016). GW150914: First Results from the Search for Binary Black Hole Coalescence with Advanced LIGO. *Phys. Rev. D* 93, 122003.
- [39] LIGO Virgo Collaboration. (2016). The Rate of Binary Black Hole Mergers Inferred from Advanced LIGO Observations Surrounding GW150914. *Accepted Astrophys. J. Lett*
- [40] LIGO Virgo Collaboration. (2016). Astrophysical Implications of the Binary Black-Hole Merger GW150914. *Astrophys. J. Lett* 818, L22.
- [41] LIGO Virgo Collaboration. (2016). Tests of General Relativity with GW150914. *Phys. Rev. Lett.* 116, 221101.
- [42] LIGO Virgo Collaboration. (2016). GW150914: Implications for the Stochastic Gravitational Wave Background from Binary Black Holes. *Phys. Rev. Lett.* 116, 131102.
- [43] LIGO Virgo Collaboration. (2016). Calibration of the Advanced LIGO Detectors for the Discovery of the Binary Black-hole Merger GW150914. *Submitted to Phys. Rev. D*.
- [44] LIGO Virgo Collaboration. (2016). Characterization of Transient Noise in Advanced LIGO Relevant to Gravitational Wave Signal GW150914. *Class. Quant. Grav.* 33, 134001.
- [45] LIGO Virgo Collaboration and ANTARES and IceCube Collaborations. (2016). High-energy Neutrino Follow-up Search of Gravitational Wave Event GW150914 with ANTARES and IceCube. *Phys. Rev. D* 93 122010.
- [46] LIGO Virgo Collaboration. (2016). GW150914: The Advanced LIGO Detectors in the Era of First Discoveries. *Phys. Rev. Lett.* 116, 131103.

- [47] LIGO Virgo, ASKAP, BOOTES, Dark Energy Survey and Camera, GW-EM, Fermi GBM and LAT, GRAWITA, INTEGRAL, IPTF, InterPlanetary, J-GEM, La Silla-Quest, Liverpool Telescope, LOFAR, MASTER, MAXI, MWA, PAN-STARRS, PESSTO, PI of the Sky, SkyMapper, Swift, TAROT, Zadko, Algerian National Observatory, C2PU, TOROS, and VISTA Collaborations. (2016). Localization and Broadband Follow-up of the Gravitational-wave Transient GW150914. *Astrophys. J. Lett.* 826, L13.
- [48] Bambi, Cosimo. (2017) Testing black hole candidates with electromagnetic radiation. *Reviews of Modern Physics* 89.
- [49] Martynov, D.V., et al. (2016). Sensitivity of the Advanced LIGO detectors at the beginning of gravitational wave astronomy. *Phys. Rev. D* 93, 112004.
- [50] Poisson, Eric; Pound, Adam; Vega, Ian. (2011). The motion of point particles in curved spacetime. *Living Reviews in Relativity.* 14, 7.
- [51] Hesthaven, Jan S.; Warburton, Tim. (2008). *Nodal Discontinuous Galerkin Methods: Algorithms, Analysis, and Applications*. Springer.
- [52] Saulson, Peter R. (1994). *Fundamentals of Interferometric Gravitational Wave Detectors*. World Scientific Publishing Co.
- [53] Press, William H.; Teukolsky, Saul A.; Vetterling, William T.; Flannery, Brian P. (2002). *Numerical Recipes in C++: The Art of Scientific Computing*. The Press Syndicate of the University of Cambridge.
- [54] Wolfram, Stephen. (2016). *An Elementary Introduction to the Wolfram Language*. Wolfram-Media, inc.
- [55] Newman, Mark. (2013). *Computational Physics*. University of Michigan.
- [56] Wald, Robert M. (1984). *General Relativity*. The University of Chicago.
- [57] Carroll, Sean M. (2004). *An Introduction to General Relativity Spacetime and Geometry*. Addison Wesley.
- [58] Misner, Charles W.; Thorne, Kip S.; Wheeler, John Archibald. (1973). *Gravitation*. W. H. Freeman and Company.

Vita

My past research has been on comet photometry, x-ray bursts, gravitational lensing and cosmology, exoplanets, neutrino oscillations, theoretical particle physics, gravitational waves, gravity gradient noise, and fractional calculus. Most of my background is in simulation, whether statistical or theoretical. I think of myself as a computational physicist and a multimessenger astronomer. If we can consider my various meanderings as one path toward these two goals, I have been walking this path for more than a decade.

I have 27 publications or preprints thanks in part to my membership in the LIGO Scientific Collaboration from 2009 to 2011. I made significant contributions to four or five of these, three or four related to LIGO and one related to exoplanets. I have also had the opportunity to submit, unsuccessfully, an additional first author paper on the simulation of digital fractional order circuit devices with Gary Bohannon at Saint Cloud State University.

Now I am a fourth year graduate student at Louisiana State University, exactly where I intended to be. I have worked on LIGO during the time of three detections. I have had the opportunity to gain experience with multiple techniques for speeding up code with supercomputers. I have done a little research involving databases and more involving numerical algorithms. I continue to contribute to the field of general relativity and to participate in a department where my broad background in the connections between various fields of astronomy is valued. I have helped supervise undergraduate research progress and made a lesson plan for and taught a graduate class, once. This document contains the research I have produced in the last three years since I arrived on June 3, 2014 at LSU and began working with Peter Diener. These have been the best three years of my life.

When interpreting the name on this document, please understand that I am female to male transgendered and that my legal name is Susan Elaine Dorsher but that I go by Steven James Dorsher.